Results in Physics 35 (2022) 105340

Contents lists available at ScienceDirect

Results in Physics

journal homepage: www.elsevier.com/locate/rinp

Role of the surface effects and interparticle magnetic interactions in the temperature evolution of magnetic resonance spectra of ferrihydrite nanoparticle ensembles

D.A. Balaev [a,b,*], S.V. Stolyar [a,b,c], Yu.V. Knyazev [a,*], R.N. Yaroslavtsev [a,c], A.I. Pankrats [a,b], A. M. Vorotynov [a], A.A. Krasikov [a], D.A. Velikanov [a], O.A. Bayukov [a], V.P. Ladygina [c], R. S. Iskhakov [a]

[a] Kirensky Institute of Physics, Federal Research Center KSC SB RAS, Akademgorodok 50, bld. 38, Krasnoyarsk 660036, Russia
[b] Siberian Federal University, Svobodniy 79, Krasnoyarsk 660041, Russia
[c] Krasnoyarsk Scientific Center, Federal Research Center KSC SB RAS, Akademgorodok 50, Krasnoyarsk 660036, Russia

ARTICLE INFO

Keywords:
Ferrihydrite nanoparticles
Superparamagnetism
Interparticle magnetic interactions
Ferromagnetic resonance

ABSTRACT

Ferrihydrite is characterized by the antiferromagnetic ordering and, in ferrihydrite nanoparticles, as in nanoparticles of any antiferromagnetic material, an uncompensated magnetic moment is formed. We report on the investigations of ferrihydrite powder systems with an average particle size of ~ 2.5 nm obtained (i) as a product of the vital activity of bacteria (sample FH-bact) and (ii) by a chemical method (sample FH-chem). In the first approximation, these samples can be considered to be identical. However, in sample FH-chem, particles contact directly, while in sample FH-bact, they have organic shells; therefore, the interparticle magnetic interactions in these samples have different degrees. The main goal of this work has been to establish the effects of the interparticle magnetic interactions and individual characteristics of ferrihydrite nanoparticles on ferromagnetic resonance (FMR) spectra. The FMR spectra have been measured at different (9.4–75 GHz) frequencies in a wide temperature range. It has been found that, at low temperatures, the field-frequency dependence $\nu(H_R)$ of the investigated systems has a gap $\nu/\gamma = H_R + H^A$, where H_R is the resonance field and H^A is the induced anisotropy, which decreases with increasing temperature. To estimate a degree of the effect of interparticle interactions on the results obtained and to correctly determine the temperature range of the superparamagnetic (or blocked) state, the static magnetic measurement and Mössbauer spectroscopy data have been obtained and analyzed. It has been shown that the most striking feature of the FMR spectra - a gap in the field-frequency dependences - is a manifestation of individual characteristics of ferrihydrite nanoparticles. The induced anisotropy is caused by freezing of a subsystem of surface spins and its coupling with the particle core, which is observed in both samples at a temperature of ~80 K. The temperature range (below 80 K) in which the gap exists corresponds to the blocked state in the FMR technique. In sample FH-bact, the ratio between the FMR parameters H^A and linewidth ΔH obeys the standard expression $H^A \sim (\Delta H)^3$. In sample FH-chem, however, the interparticle magnetic interactions dramatically affect the behavior of parameters of the FMR spectra, which change nonmonotonically upon temperature variation. This fact is attributed to the collective freezing of the magnetic moments of particles under the conditions of sufficiently strong interactions, which follows from the temperature dependence of the particle magnetic moment relaxation time determined from the Mössbauer spectroscopy and static magnetometry data obtained in weak magnetic fields.

Introduction

At present, the ranges of application of magnetic nanoparticles and composite systems based on them are being steadily extended. These materials can be used in medicine (drug delivery, magnetic hyperthermia) [1–5], environmental engineering [6,7], high-density nonvolatile memory [8–10], catalysis [11–14], etc. This stimulates an intense search for new methods for synthesizing systems based on ensembles of

* Corresponding authors.
E-mail addresses: dabalaev@iph.krasn.ru (D.A. Balaev), yuk@iph.krasn.ru (Yu.V. Knyazev).

https://doi.org/10.1016/j.rinp.2022.105340
Received 12 January 2022; Accepted 12 February 2022
Available online 16 February 2022

magnetic nanoparticles and their comprehensive study. Along with the well-studied iron oxide nanoparticles (see, for example, [15,16]), iron hydroxides are being widely investigated. A bright representative of hydroxides is ferrihydrite, which is examined in this work.

Ferrihydrite with a nominal formula $Fe_2O_3{\cdot}nH_2O$ existing only on the nanoscale is widespread in aqueous systems and plays an important role in the vital activity of microorganisms and higher animals. In organisms of higher animals, it is contained in ferritin, which is a ferrihydrite nanocrystal enclosed in a protein shell. The magnetic moments of iron atoms in ferrihydrite are ordered antiferromagnetically (AFM) and, according to the data reported in [17], the Néel temperature is ~ 340 K. The AFM magnetic ordering suggests a fairly weak response to a magnetic field. However, as predicted by Néel [18], structural defects, which inevitably exist in AFM nanoparticles, cause partial decompensation of the magnetic sublattices and, consequently, possible occurrence of the uncompensated magnetic moment μ_{un} of AFM particles. This hypothesis was confirmed in many works on studying various AFM nanoparticle systems [19–34], including ferrihydrite. Here, typical values of the saturation magnetization reduced to the mass of an AFM material are around 1–10 emu/g and the μ_{un} value for AFM particles several nanometers in size attains hundreds of Bohr magnetons [19–40]. These magnetic characteristics, together with the discovered nontoxicity of hydroxides for animals and the antibacterial properties of ferrihydrite [41], allow one to speak about a high potential of this nanomaterial, in particular, for biomedicine [42–44].

At an average particle size of several nanometers, which is characteristic of investigated ferrihydrite systems, the surface effects are especially bright. Concerning the magnetic properties, this is expressed, first of all, in the growth of the magnetic anisotropy due to the contribution of the surface magnetic anisotropy [45–48]. Another surface effect is the occurrence of an additional magnetic subsystem formed by surface spins. Upon cooling, this subsystem can pass into the spin glass state; in this case, the exchange coupling between the surface spins and spins of the particle core serves as an additional source of the magnetic anisotropy [49–52,22,25,53–58]. However, to verify the surface effects, it is necessary to elucidate the impact of interparticle magnetic interactions (hereinafter referred to as IPIs) on the magnetic characteristics of powder systems. The IPIs can lead, in particular, to an increase in the temperature of the transition to the unblocked, i.e., superparamagnetic (SPM) state [59–61,40,62–64]; this collective effect is hard to distinguish from, e.g., the growth of the nanoparticle magnetic anisotropy caused by the surface magnetic anisotropy in an individual nanoparticle. It is clear that the IPIs in powder systems coexist with the surface effects in an individual nanoparticle, which strongly complicates understanding of the mechanisms responsible for the magnetic characteristics of nanoparticle ensembles. To reliably identify the magnetic state of such powder systems, it is reasonable to use experimental techniques with different characteristic measurement times and to study samples with different degrees of the IPI effect.

Among several available techniques, we can choose ferromagnetic resonance (FMR), the characteristic measurement time of which is rather short (inversely proportional to the microwave radiation frequency). The FMR method was used in many studies on various nanoparticle systems [52,53,60,65–80], including ferrihydrite ones [81–86,58]. An analysis of the temperature evolution of resonance field H_R made it possible to identify the transition of the surface spin subsystem to the spin glass-like state [52,53,58]. At the same time, the FMR results are sometimes difficult to unambiguously interpret, in contrast, for example, to the static magnetometry data. For the latter, the transition to the SPM state can be clearly identified, whereas the FMR method has no universal and commonly accepted criterion for identifying the SPM state. The FMR study is generally carried out in the X-band frequency range because of the standardization of experimental facilities and the widespread use of spectrometers operating in this range. The measurements of the field-frequency dependences $\nu(H_R)$ or the temperature evolution of parameters of FMR spectra at different frequencies may appear more informative [76–79,81,58]. In this case, however, a comparison with the data obtained by other techniques must be made.

The aim of this study was to establish features of FMR spectra of ferrihydrite nanoparticle ensembles with different degrees of the IPI effect. For this purpose, the FMR spectra were recorded at different frequencies (9.4–75 GHz) and temperatures (4.2–300 K). Two investigated samples were powder systems of chemical and biogenic ferrihydrite. In chemical ferrihydrite, particles contact directly and, for this sample, the presence of the IPI was confirmed in [87] by both Mössbauer spectroscopy and static magnetometry. In biogenic ferrihydrite, particles have an organic shell, so the IPIs are partially screened [88–90].

The article is organized as follows. Section 2 describes the synthesis method and experimental techniques used. Section 3 presents the results of morphological characterization, static magnetic properties, and FMR and Mössbauer spectroscopy data. In Section 4, temperatures T_B of the transition to the SPM state are analyzed for the static magnetic properties and Mössbauer spectroscopy data, the particle relaxation times obtained from the Mössbauer spectra are discussed, and the T_B-H diagram for the static magnetic properties is analyzed. Further, the T_B-H diagram is extended to the magnetic resonance conditions, which allows us to draw conclusions about the FMR spectrum features reflecting individual properties of particles and about the properties caused by the IPI effect. The aforesaid is summarized in Section 5.

Experimental

Chemical ferrihydrite FH-chem was synthesized at room temperature by adding slowly a solution of alkali NaOH (1 M) at a rate of 0.01–0.001 mol/min to a solution of ferric chloride $FeCl_3$ (0.02 M) under constant stirring until neutral pH. The precipitate formed was collected on a filter, washed, and dried at room temperature.

The biogenic ferrihydrite sample was obtained by isolation from bacterial sediments after cultivating *Klebsiella oxytoca* bacteria under anaerobic conditions, as described in [88,89,41,90]. The resulting dried sol is an aggregated system of fine (about 2–3 nm in size) ferrihydrite nanoparticles coated with an organic shell [89,90]. The biogenic ferrihydrite sample is hereinafter referred to as FH-bact.

The electron microscopy investigations were carried out on a Hitachi HT7700 transmission electron microscope at an accelerating voltage of 100 kV. Specimens were prepared by shaking the nanoparticle powder in alcohol in an ultrasonic bath and depositing the obtained suspension onto support meshes with a perforated carbon coating.

The temperature dependences of the magnetization M(T) were measured on a SQUID magnetometer in the external field range of 1–1000 Oe [91] and on a vibrating sample magnetometer (VSM) [92] in fields of 1–50 kOe. The zero field cooling (ZFC) and field cooling (FC) modes were used. The M(H) dependences in fields of up to 60 kOe were obtained on a VSM [91]. In the magnetic measurements, the powder was fixed in a measuring capsule in paraffin. The data on the magnetic moment are given in emu units per powder unit mass.

The X-band FMR spectra were recorded on a Bruker ELEXSYS 560 spectrometer at a microwave radiation frequency of ~ 9.4 GHz in the temperature range of 110–300 K. The FMR spectra at frequencies of 25–75 GHz were obtained on an original setup [93], which makes it possible to obtain absorption spectra by a pulsed magnetic field sweep with a pulse length of 12 ms in a wide temperature range starting from 4.2 K. In these measurements, the test powder was fixed in epoxy resin.

The Mössbauer spectra were obtained on an MS-1104Em spectrometer manufactured at the Research Institute of Physics, Southern Federal University (Russia) in the transmission geometry with a Co^{57}(Rh) radioactive source in the temperature range of 4–300 K using a CFSG-311-MESS cryostat with a sample in the exchange gas based on a closed-cycle Gifford-McMahon cryocooler (Cryotrade Engineering). The spectra were processed by varying the entire set of hyperfine parameters by the least-squares method in the linear approximation. The relaxation

times of the nanoparticle magnetic moments were determined using the model proposed in [94,95].

Results

Microstructure characterization

Fig. 1 shows typical photomicrographs and particle size distributions. The comparison of the histograms in Fig. 1 shows that the particle size distributions are similar. Average particle sizes $< d >$ for samples FH-chem and FH-bact were 2.7 and 2.4 nm, respectively. It is noteworthy that the maximum particle sizes in the two samples are also similar: $d_{max} \approx 3.3$ nm. The results obtained allowed us to compare the characteristics of samples FH-chem and FH-bact.

Magnetic properties

Fig. 2a shows the M(T) dependences for the investigated samples obtained in the ZFC mode and in the FC mode in a field of H = 100 Oe. The $M(T)_{ZFC}$ dependences have maxima T_{max}. The T_{max} values are ≈24 and ≈44 K for samples FH-bact and FH-chem, respectively. At temperatures far above T_{max}, the $M(T)_{ZFC}$ and $M(T)_{FC}$ dependences diverge (in Fig. 2, $T_{irr} \approx T_{max}$, where T_{irr} is the temperature of the irreversible $M(T)_{ZFC}$ and $M(T)_{FC}$ behavior). This behavior is typical of the SPM blocking. For such processes, in the unblocked region $T > T_B$ in a relatively weak external field, we can expect a temperature decrease in the magnetization proportional to 1/T. Indeed, this behavior is observed for sample FH-bact, which is illustrated in the inset to Fig. 2, where the data are given in the coordinates (M^{-1}, T). For sample FH-chem, however, a linear dependence of M^{-1} on T cannot be seen. The presence of IPIs in chemical ferrihydrite was confirmed previously in [87]; therefore, the discrepancy between the $M(T) \sim 1/T$ dependence can be explained here by the fact that each particle is in an effective field representing a superposition of the external field H and the interaction field induced by the magnetic moments of surrounding particles. This effective field does not stay constant upon temperature variation, which leads to the deviation from the canonical dependence $M(T) \sim 1/T$. Another reason may be the effect of the temperature dependence of the magnetic susceptibility of the particles core (see below). The effect of an external field on the temperature of the transition to the SPM state is analyzed in Section 4.2.

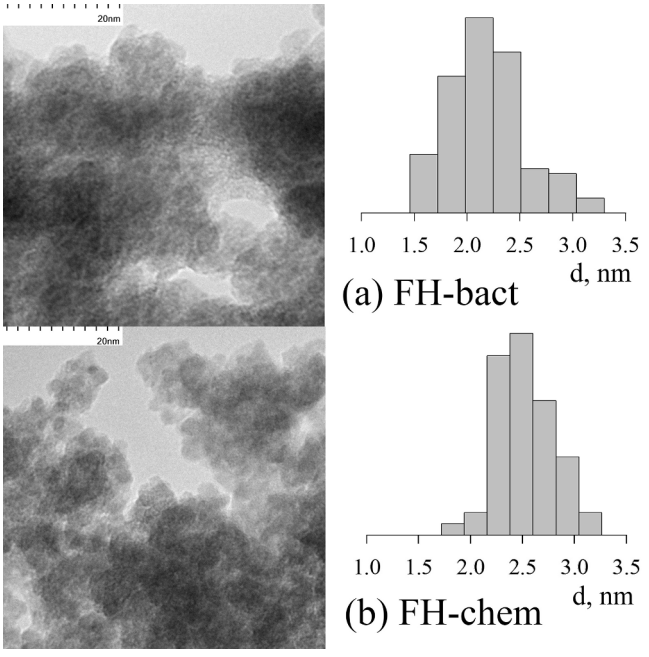

Fig. 1. Typical TEM images and particle size distributions for samples (a) FH-bact and (b) FH-chem.

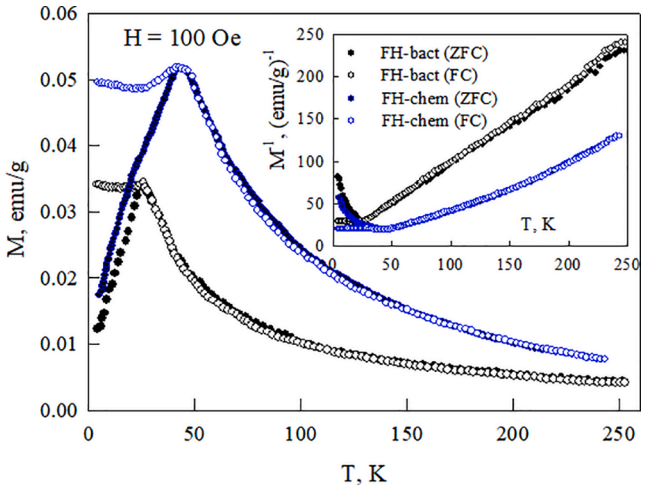

Fig. 2. M(T) dependences for the ferrihydrite samples obtained in the ZFC mode and in the FC mode in a field of H = 100 Oe. Inset: the same in coordinates (M^{-1}, T). The legend corresponds to both the figure and the inset.

Fig. 3a shows the M(H) hysteresis loops for the samples at T = 4.2 K. The loops are typical of AFM nanoparticles, for which the magnetization curve can be described by a sum of two terms: $M_{FM}(H)$ and $\chi \cdot H$. The term $M_{FM}(H)$ reflects the arrangement of uncompensated magnetic moments μ_{un} of particles along the external field and χ includes the AFM susceptibility and other possible contributions [19–23,26–34]. According to the data presented in Fig. 3a, there is some difference between the χ values of the investigated samples, if we roughly define this quantity as a slope of the M(H) dependences in the strong-field region. The samples have different coercivities H_C (see the inset to Fig. 3a): $H_C \approx 4$ kOe for sample FH-chem and $H_C \approx 2.2$ kOe for sample FH-bact. As was noted in experimental [61,96,97] and theoretical studies [98,99], the presence of IPIs can lead to an increase in H_C in the systems with identical properties of individual particles.

Fig. 3b and 3c show the experimental M(H) dependences for samples FH-bact and FH-chem, respectively. The isotherms correspond to the temperature range of the SPM state (the measurement temperatures are known to exceed T_{irr}). To determine the μ_{un} and χ values, the experimental M(H) dependences were fitted by the equation

$$M(H) = N_P \int_0^\infty L(\mu_{un}, H)\, f(\mu_{un})\, \mu_{un}\, d\mu_{un} + \chi \cdot H. \quad (1)$$

Here, N_P is the number of particles per unit sample mass and $L(\mu_{un}, H)$ is the Langevin function: $L(\mu_{un}, H) = \coth(\mu_P \cdot H / kT) - 1/(\mu_{un} \cdot H/kT)$, where k is the Boltzmann constant. As in [23,27–30,32–34,38], $f(\mu_{un})$ was the lognormal distribution $f(\mu_{un}) = (\mu_{un} \cdot s \cdot (2\pi)^{1/2})^{-1} \exp\{-[\ln(\mu_{un}/n)]^2/2s^2\}$. In this distribution, $<\mu_{un}> = n \cdot \exp(s^2)$ is the average magnetic moment of a particle and s^2 is the $\ln(\mu_{un})$ dispersion. When fitting, the N_P and s values remained constant (for a specific sample) and only the n values (they determine $< \mu_{un} >$) and χ values changed with temperature. Solid lines in Fig. 3b, 3c show the best fit to Eq. (1).

The agreement between the experimental and fitting M(H) dependences in Fig. 3b, 3c was obtained at $N_P = 3.2 \cdot 10^{18}$ and $3.8 \cdot 10^{18}$ for samples FH-bact and FH-chem, respectively. The temperature evolution of the fitting parameters $< \mu_{un} >$, M_{FM}, and χ is illustrated in Fig. 4. The M_{FM} value corresponds to the value of the first term in Eq. (1) at a strong external field; i.e., this is, in fact, the saturation magnetization of the ferromagnetic subsystem. The $< \mu_{un} >(T)$ dependence is shown in Fig. 4a, in which solid curves correspond to the fitting by the function

$$<\mu_{un}>(T) = <\mu_{un}>(T = 0) \cdot (1 - b \cdot T^a), \quad (2)$$

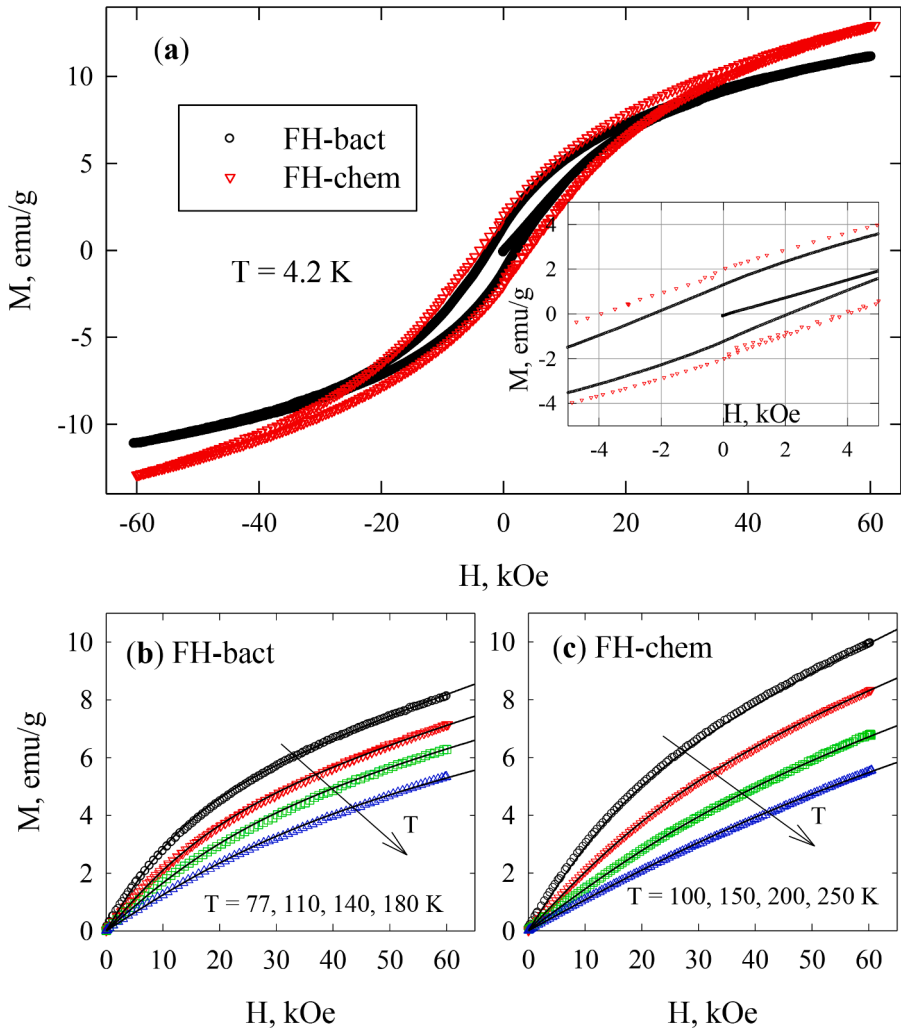

Fig. 3. M(H) dependences for the ferrihydrite samples. (a) Magnetization hysteresis at T = 4.2 K. Inset: enlarged scale near the origin of coordinates. M(H) dependences for samples (b) FH-bact and (c) FH-chem at different temperatures (indicated in the figures). Symbols correspond to the experiment and solid curves, to the best fitting by Eq. (1).

where b is the constant. This function describes satisfactorily the data obtained for both samples at $a = 1.5$. We note that, for different AFM samples of ferrihydrite, ferritin, and NiO nanoparticles, dependence (2) was observed at exponents a from 1.5 to 2 [21,23,30,31–34].

The $<\mu_{un}>(T = 0)$ values for the two samples appeared to be similar (173 and 176 μ_B for FH-bact and FH-chem, respectively; μ_B is the Bohr magneton). The similarity of these values is consistent with approximately the same size distributions (Fig. 1) and similar average sizes (Section 3.1). A slightly lower M_{FM} value for sample FH-bact (Fig. 4b) is determined by a smaller N_P value. This is possibly due to the presence of an organic shell on biogenic ferrihydrite particles. The noticeably higher experimental values of the FH-chem magnetization (compare the data in Fig. 3a and Fig. 4b, 4c at similar temperatures) are determined by the higher susceptibility χ (see Fig. 3c). This is consistent also with the larger slope (~dM/dH) of the M(H) dependence for sample FH-chem in Fig. 3a. It should be noted that the χ(T) dependence for AFM nanoparticles can reflect not only the temperature evolution of the AFM susceptibility of the corresponding bulk AFM material, but also the field-linear contribution of the small magnetic moments [100,101], the subsystem of surface paramagnetic spins [30,34,100], and the super-antiferromagnetic susceptibility [102,100,30,31,34].

The obtained values $<\mu_{un}>(T = 0) \approx 173–176\ \mu_B$ allow us to find the number N_{un} of the uncompensated magnetic moments μ_{Fe} of iron atoms in an average-size particle. For trivalent iron (recall that Fe^{3+} forms ferrihydrite, see Section 3.4), we have $\mu_{Fe} \approx 5\ \mu_B$; consequently, $N_{un} \approx 35$. For a spherical ferrihydrite particle ~ 2.5 nm in size, the total number N_{Fe} of Fe atoms will be ~ 700. This ratio between N_{un} and N_{Fe} agrees well with the Néel hypothesis [18], according to which, in the case of defects both on the surface and in the bulk of an AFM particle, we have $<\mu_{un}> \approx \mu_{Fe} \cdot N_{un} \sim \mu_{Fe} \cdot N_{Fe}^{0.5}$. The resulting ratio is typical of ferrihydrite and ferritin particles [20–23,27,28], as well as NiO ones [30,34].

Summarizing the results presented in Section 3.2, we can state that the magnetic characteristics of individual particles in the two samples are similar, which is no surprise, taking into account the identity of the atomic structures and particle size distributions. At the same time, the transition to the SPM state for sample FH-chem occurs at a noticeably higher temperature; this sample also has a higher coercivity at T = 4.2 K. These facts result from the effect of IPIs in the chemical ferrihydrite powder system.

Ferromagnetic resonance

X-band resonance

Fig. 5 presents the FMR spectra of the investigated samples obtained at temperatures from 110 to 300 K. The spectra are single Lorentzian lines. The resonance fields remain almost unchanged upon temperature variation (dashed lines in Fig. 5). The temperature dependences of the

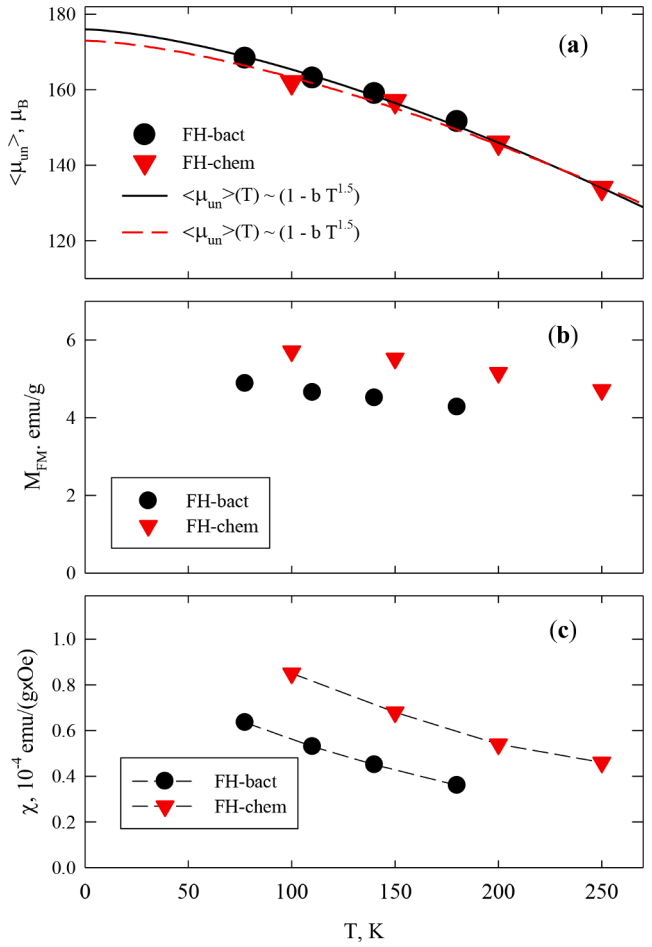

Fig. 4. Temperature evolution of the parameters obtained by processing the data from Fig. 3b, 3c using Eq. (1). (a) Uncompensated magnetic moment $<\mu_{un}>$ (symbols); solid curves are built using Eq. (2). (b) Saturation magnetization $M_{FM}(T)$ corresponding to $<\mu_{un}>$. (c) Susceptibility χ according to Eq. (1).

linewidth ΔH and integrated intensity I (normalized to the value at T = 300 K) are shown in Fig. 6a. The linewidth increases monotonically with a decrease in temperature, which is apparently due to an increase in the local fields in the samples with decreasing temperature. It is noteworthy that the linewidth for sample FH-chem is noticeably larger than that for sample FH-bact. Taking into account the similarity of the magnetic characteristics of individual particles (Section 3.2) and the absence of visible differences in their morphology (Section 3.1), we can conclude that the IPIs lead to an increase in the FMR linewidth.

The intensity of lines monotonically increases with decreasing temperature (Fig. 6a). This parameter is proportional to the magnetization and sometimes the nonmonotonic behavior was observed for the

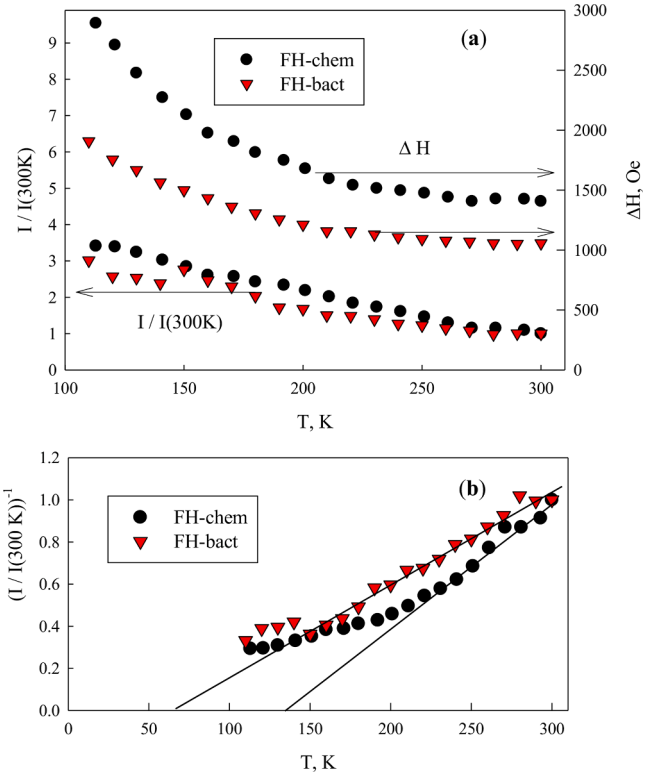

Fig.6. (a) – Temperature dependences of linewidth ΔH (the right-hand scale is the Y axis) and integral intensity I (the left-hand scale is the Y axis) of the FMR spectra according to the data from Fig. 5. (b) – Temperature dependence of the inverse intensity $I^{-1}(T)$. Straights correspond to the approximation of the results by the dependence I(T) ~ 1/T at high temperatures.

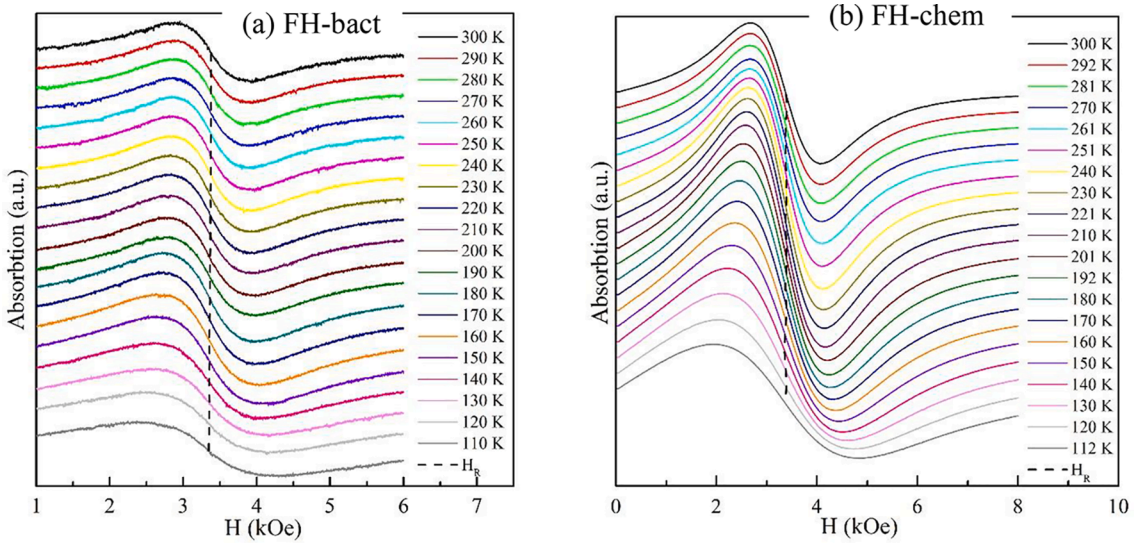

Fig. 5. FMR spectra at a frequency of 9.4 GHz for samples (a) FH-bact and (b) FH-chem at the indicated temperatures.

systems of nanoparticles [72,75,76,82,84,85] (the presence of a maximum), which was interpreted as a transition of the magnetic moments of particles to the SPM state. In this case, the I(T) dependence proportional to 1/T can be a sign of the SPM state for sufficiently high temperatures [67]. In the investigated case, we can state that, for sample FH-bact, in the temperature range above 150 K, the dependence I(T) ~ 1/T + const is observed. This is illustrated in Fig. 6b, which shows the $I^{-1}(T)$ dependences. The non-strict correspondence of the functional 1/T dependence can be caused by the second term in Eq. (1) or by other reasons. For sample FH-chem, the dependence I(T) ~ 1/T is less pronounced (see Fig. 6b) and the range where this dependence can be distinguished begins at a higher (~240 K) temperature. The ratio between the indicated temperatures (150 and 240 K) correlates well with the ratio between the T_{max} values of the $M(T)_{ZFC}$ dependences (24 and 45 K for samples FH-bact and FH-chem, respectively), taking into account different FMR and magnetometry characteristic measurement times. Nevertheless, it is difficult to unambiguously determine the temperatures of the transition from the blocked to SPM state under the FMR conditions without additional analysis. Thus, there is a difference in the absolute values of ΔH and in the temperature behavior of the integral FMR intensity for the samples under study.

Ferromagnetic resonance at frequencies of up to 75 GHz

Fig. 7 shows the FMR absorption lines for the two samples obtained at different temperatures and a frequency of 75 GHz. Even a qualitative comparison of the spectra of samples FH-bact (Fig. 7a) and FH-chem (Fig. 7b) shows that, at least at temperatures above ~ 100 K, the linewidth for biogenic ferrihydrite is noticeably narrower. This is consistent with the data obtained at 9.4 GHz (Fig. 6a), but there are some differences. The temperature dependence of the resonance field (dashed curves in Fig. 7) is observed: in the temperature range of 80–150 K, the resonance field is constant ($H_R \approx$ const), while at low temperatures, H_R decreases with temperature; this decrease is monotonic for sample FH-bact and the $H_R(T)$ dependence is nonmonotonic for sample FH-chem.

Fig. 8 shows the $\nu(H_R)$ dependences obtained at T = 4.2 K and at high (above 100 K) temperatures. At T = 4.2 K, the $\nu(H_R)$ dependence has a gap caused by the induced anisotropy and can be described as $\nu/\gamma = H_R + H^A$, where γ is the gyromagnetic ratio and H^A is the induced anisotropy field, which is ~ 8.3 and ~ 13.5 kOe for samples FH-bact and FH-chem, respectively. It can be seen in Fig. 8 that, in the temperature range of 100–150 K, the gap (induced anisotropy) vanishes: $H^A = 0$.

Fig. 9 shows the temperature dependences of the resonance fields $H_R(T)$ for the examined samples. The data obtained at different frequencies (including the results obtained in 3.3.1) are presented. These

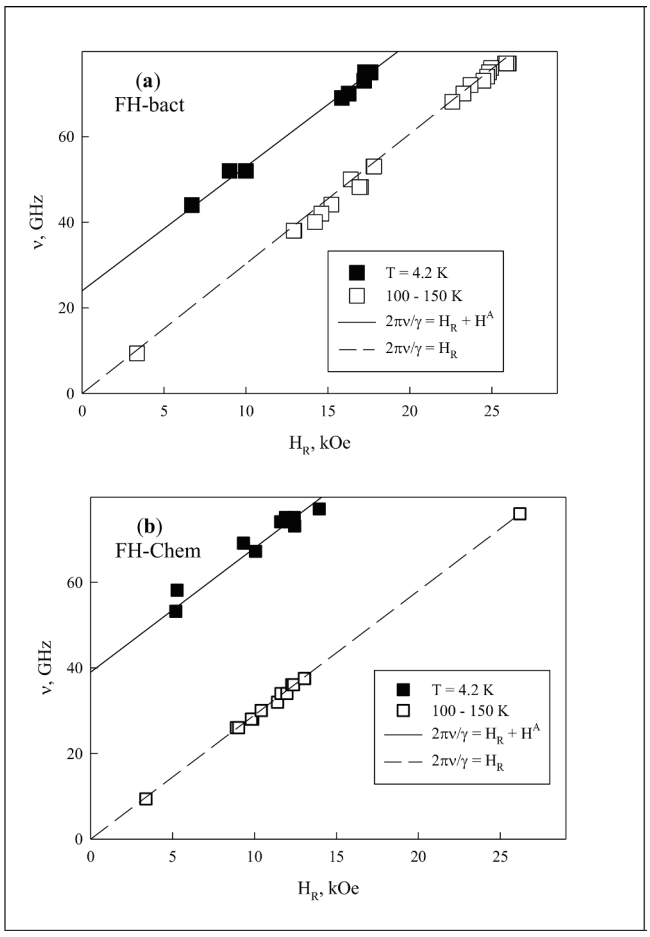

Fig. 8. Field-frequency dependences $\nu(H_R)$ for samples (a) FH-bact and (b) FH-chem at the indicated temperatures. Symbols correspond to the experiment and straights, to the legends.

dependences reflect the evolution of the induced anisotropy field H_A (or the gap in the $\nu(H_R)$ dependences, Fig. 8) upon temperature variation. It appears at the temperatures marked by the asterisk in Fig. 9 and increases with decreasing temperature. The temperatures of the occurrence of the induced anisotropy are approximately the same for the two samples and lie between 60 and 80 K. In Fig. 9b, the nonmonotonic

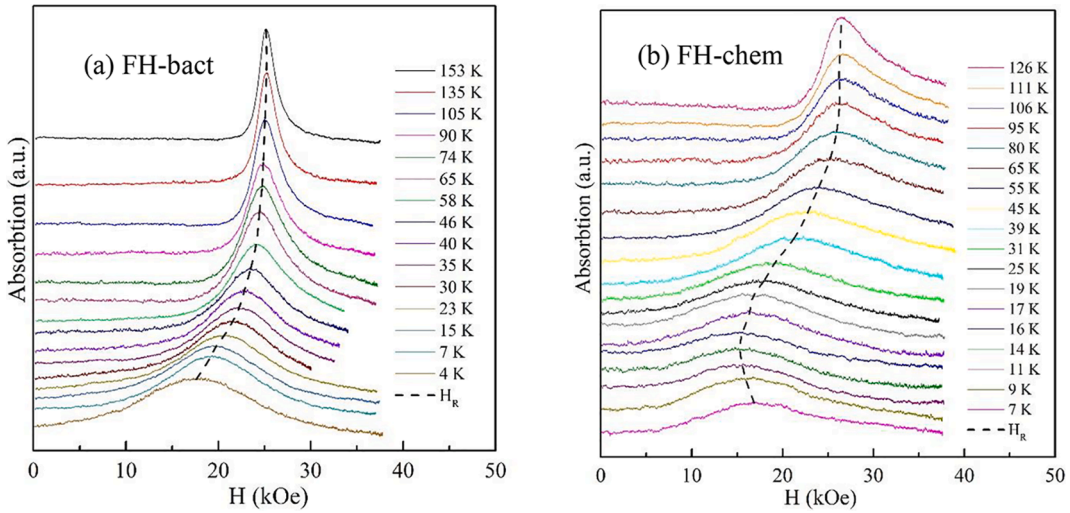

Fig. 7. FMR spectra at a frequency of 75 GHz for samples (a) FH-bact and (b) FH-chem at the indicated temperatures.

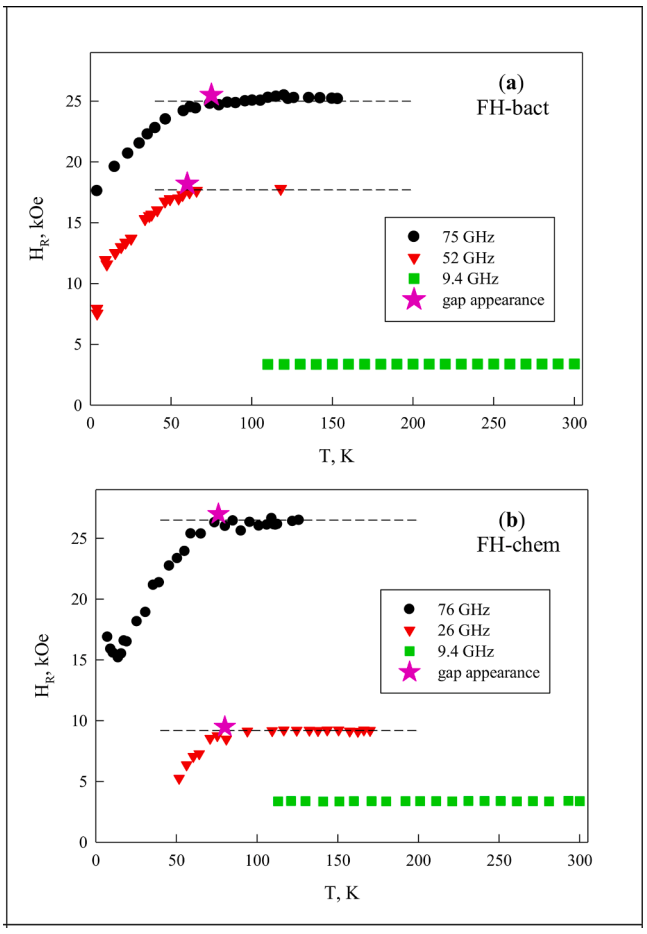

Fig. 9. Temperature dependences of resonance field H_R at the indicated microwave frequencies for samples (a) FH-bact and (b) FH-chem. Horizontal dashed lines correspond to constant H_R at sufficiently high temperatures.

H_R(T) behavior (for the data at $\nu = 75$ GHz) of sample FH-chem at low temperatures can be seen. It is fairly difficult to determine from the shape of the spectra in Fig. 7, as in the case of the X-band FMR data (Section 3.3.1), at which temperature the transition to the blocked state occurs.

Mössbauer spectroscopy

Fig. 10 shows typical Mössbauer spectra of the samples obtained at different temperatures. At room temperature, the spectra of both samples are a doublet consisting of three components corresponding to the three nonequivalent positions of a ferric iron in ferrihydrite [7,66–69]. As applied to the magnetic moments of nanoparticles, the doublet is indicative of the SPM state of the particle magnetic moments. Iron cations are in the high-spin trivalent state in all the positions. The ratios between the occupancies of these doublets in the spectra of both samples are almost identical and close to 3 : 2 : 1, which remains almost unchanged over the entire temperature range (Tables 1 and 2). A decrease in temperature leads to the occurrence of a hyperfine spectral structure. In this case, the relaxation component in the form of a single broad non-Lorentzian line appears in the spectra. This is indicative of the magnetic interactions between particles [103–105]. The Mössbauer spectra reveal the complete Zeeman splitting (sextets) only at temperatures below 20 K

Table 1
Mössbauer parameters of chemical ferrihydrite nanoparticles – sample FH-chem. IS is the chemical shift relative to α-Fe, H_{hf} is the hyperfine field at iron nuclei, QS is the quadrupole splitting, W is the width of the Mössbauer line at half maximum, τ is the calculated relaxation time of the magnetic moment. A - relative occupancy of the position.

	IS, ±0.005 mm/s	H_{hf}, ±3 kOe	QS, ±0.01 mm/s	W, ±0.01 mm/s	$\tau_0 \times 10^{-8}$, s	A, ±0.03 %
4 K						
1	0.512	512	0	–	4.0	0.47
2	0.498	485	0	–	4.9	0.34
3	0.47	452	0	–	4.8	0.18
40 K						
1	0.506	430	0	–	2.0	0.48
2	0.5	368	0	–	2.2	0.30
3	0.506	255	0	–	1.9	0.23
50 K						
1	0.452	368	0.008	–	1.2	0.46
2	0.462	269	0	–	1.4	0.34
3	0.511	186	0	–	1.8	0.20
65 K						
1	0.482	253	0.067	–	0.19	0.99
80 K						
1	0.477	117	0.00	–	0.08	0.32
1	0.476	–	0.65	0.43	–	0.28
2	0.484	–	1.14	0.43	–	0.24
3	0.478	–	1.68	0.56	–	0.16
95 K						
1	0.358	–	0.47	0.37	–	0.45
2	0.361	–	0.82	0.30	–	0.38
3	0.373	–	1.17	0.32	–	0.17

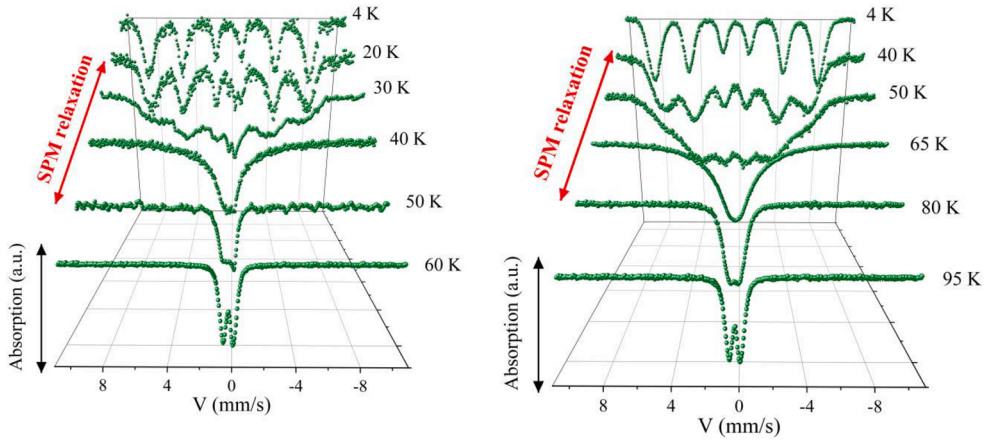

Fig. 10. Mössbauer spectra of samples (a) FH-bact (on the left) and (b) FH-chem (on the right) at the indicated temperatures. The double arrow schematically shows the temperature range of existence of the relaxation component (single line).

Table 2
Mössbauer parameters of the biogenic ferrihydrite nanoparticles – sample FH-bact. IS is the chemical shift relative to α-Fe, H_{hf} is the hyperfine field at iron nuclei, QS is the quadrupole splitting, W is the width of the Mössbauer line at half maximum, τ is the calculated relaxation time of the magnetic moment. A - relative occupancy of the position.

	IS, ±0.005 mm/s	H_{hf}, ±3 kOe	QS, ±0.01 mm/s	W, ±0.01 mm/s	$\tau_0 \times 10^{-8}$, s	A, ±0.03 %
4 K						
1	0.501	508	0.00	–	5.8	0.44
2	0.503	447	0.00	–	4.7	0.19
3	0.48	480	0.00	–	5.5	0.37
20 K						
1	0.498	469	−0.07	–	4.0	0.39
2	0.525	357	0.00	–	1.6	0.29
3	0.488	426	−0.04	–	3.7	0.32
30 K						
1	0.495	425	−0.00	–	2.2	0.29
2	0.527	263	0.00	–	0.87	0.52
3	0.503	360	−0.22	–	2.7	0.19
40 K						
1	0.408	0	0.76	1.08	–	0.49
2	0.594	198	0.00	–	0.35	0.51
50 K						
1	0.383	0	0.32	0.48	0.385	0.46
2	0.523	0	1.17	0.46	0.183	0.21
3	0.377	0	0.90	0.32	0.416	0.33
60 K						
1	0.335	0	0.58	0.48	0.505	0.63
2	0.565	0	0.58	0.20	0.293	0.16
3	0.497	0	1.21	0.35	0.193	0.21

for sample FH-bact and below 40 K for sample FH-chem. The fully unblocked SPM state of the magnetic moments of particles (doublet) is observed above 60 K for sample FH-bact and above 90 K for sample FH-chem. This is in the qualitative agreement with the measured magnetization and the growth of the blocking temperature as compared with the magnetometry data is related to the shorter characteristic measurement time of the Mössbauer spectroscopy method.

Importantly, for the systems of noninteracting particles in the temperature range from the completely blocked (sextet) to SPM (doublet) state, the Mössbauer spectra can be clearly separated into corresponding partial components [106,90]. In this case, using the ratio between the partial components, which are redistributed from 100% to zero, one can determine the distribution function over the SPM blocking temperature of particles and compare it with the real particle size distribution [106,90]. In our case, this is complicated by the presence of a relaxation component and nonuniform broadening of the sextet lines.

The Mössbauer spectroscopy data obtained disclose the existence of the IPIs in both samples under study; however, for sample FH-bact, the effect of these interactions is weaker. This can be observed in the temperature ranges of existence of the relaxation component (shown by an arrow in Fig. 10). It can be seen that, for biogenic ferrihydrite, this interval is much narrower and the relaxation is observed in the range of 20–50 K, while for chemical ferrihydrite the relaxation region is much wider and lies at higher (40–90 K) temperatures.

Discussion

Evidence for different degrees of the IPI effect in the samples and nature of the transition to the blocked state

The particle relaxation time τ, for which the particle magnetic moment changes its direction under the action of thermal fluctuations, for single-domain magnetically ordered particles in the SPM state is determined by the Néel–Brown relation

$$\tau = \tau_0 \cdot \exp(K_{eff} \cdot V/kT). \quad (3)$$

Here, K_{eff} is the effective magnetic anisotropy constant, which includes the bulk magnetic anisotropy, surface magnetic anisotropy, and shape anisotropy; V is the particle volume; and τ_0 is the particle relaxation time, which can range within 10^{-9}–10^{-13} s) [103].

Using Eq. (3), the SPM blocking temperature is determined, taking into account that each experimental technique has its own characteristic measurement time τ_m, at $\tau = \tau_m$

$$T_B = K_{eff} \cdot V / \ln(\tau_m/\tau_0) \cdot k. \quad (4)$$

Samples FH-bact and FH-chem have the similar size distributions and $< d >$ and d_{max} values; the microphotographs revealed no features that would be indicative of a rod-like particle shape (see Section 3.1). Particles of these two samples have identical magnetic characteristics ($<\mu_{un}>$), see Section 3.2. The parameters of the Mössbauer spectra for the unblocked state (at T = 300 K) are similar (see Section 3.4), which suggests the identity of the local environment of iron atoms in these two samples.

Equations (3) and (4) are valid for noninteracting particles. To establish the IPI contribution, we consider the blocking temperatures in different techniques using Eq. (4). For sample FH-bact, we have $T_{BMagn} = T_{max} \approx 24$ K from the magnetic measurements (Fig. 2a) and $T_{BMöss} \approx 60$ K (Section 3.4) from the Mössbauer spectroscopy data. These temperatures can be considered to be the temperatures of the transition to the SPM state for the largest particles. In these techniques, the characteristic measurement times are $\tau_m = 10^2$ and $\tau_m = 2.5 \cdot 10^{-8}$ s, respectively. Solving a system of two equations using Eq. (4) with the T_B and τ_m values corresponding to each technique, at $K_{eff} \cdot V = const$ (this is justified by the identical properties and d_{max} values of the investigated samples), we find $\tau_0 = 10^{-14}$ s. This value is beyond the above-mentioned range, which indirectly evidences for the effect of the IPIs in sample FH-bact. For sample FH-chem, we have $T_{BMagn} = T_{max} \approx 45$ K from the magnetic measurements (Fig. 2a) and $T_{BMöss} \approx 90$ K (Section 3.4) from the Mössbauer spectroscopy data. Making the analogous estimation, we find $\tau_0 \approx 6 \cdot 10^{-18}$ s. This numerical value is already unphysically small; therefore, we can conclude that, in sample FH-chem, the IPI effect is much more pronounced than in sample FH-bact.

There exist different ways to estimate the degree of influence of the IPIs on the transition to the SPM state. If the magnetic anisotropy energy ($K_{eff}V$ is the numerator of Eq. (4)) is added with the energy U_{IPI} proportional to the degree of IPI, then Eq. (4) is rewritten in the form

$$T_B = (K_{eff} \cdot V + U_{IPI})/\ln(\tau_m/\tau_0) \cdot k. \quad (5)$$

This equation can be rewritten as

$$T_B - T_0 = K_{eff} \cdot V/\ln(\tau_m/\tau_0) \cdot k, \quad (6)$$

where the quantity $T_0 = U_{IPI}/\ln(\tau_m/\tau_0) \cdot k$ characterizes the degree of IPI. Equation (6) is known as the Vogel-Fulcher law. When estimating the T_0 values, if the blocking temperatures are known for at least two techniques with different characteristic times, it is necessary to choose a physically reasonable τ_0 value. Using the above-mentioned values $T_{BMagn} \approx 24$ K, $T_{BMöss} \approx 60$ K (sample FH-bact) and $T_{BMagn} \approx 45$ K, $T_{BMöss} \approx 90$ K (sample FH-chem) and solving the systems of two equations (6) at $\tau_0 = 10^{-12}$ s, we obtain $T_0 = 7.5$ K for sample FH-bact and $T_0 = 24.3$ K for sample FH-chem. Certainly, this is only a qualitative estimate of the IPI effect, but a threefold increase in the parameter T_0 for sample FH-chem points out a much greater role of the IPI in this sample as compared with biogenic ferrihydrite, in which particles are surrounded by a polysaccharide shell. In [107,108], a significant contribution of the IPIs to the behavior of the magnetic properties of chemical ferrihydrite was noted.

It should be noted that, for different biogenic ferrihydrite sample series (prepared at different times), the characteristic blocking temperature in the magnetic measurements in a relatively weak (100 or 1000 Oe) field ranged within 12–25 K [27,28,37,41,90]. For example, for the biogenic ferrihydrite sample studied in [90], the T_{max} value was about 12–14 K and the temperatures of the transition to the SPM state for the

magnetic measurements and the Mössbauer effect were in good agreement in the framework of Eq. (3), which is only valid for systems of noninteracting particles. For sample FH-bact studied in this work, the IPI effect can be stated. This effect, however, is much weaker than in the powder chemical ferrihydrite system, in which particles contact directly. This is consistent with the Mössbauer spectroscopy data (the appearance of a relaxation component in the spectra, Section 3.4).

In [87], the Mössbauer spectra of sample FH-chem were numerically processed using the model [94,95], which made it possible to extract the particle relaxation time. Similarly, we processed the spectra of sample FH-bact (Fig. 10a). The obtained relaxation times τ at different temperatures are shown in Fig. 11. It is noteworthy that the numerical processing of the spectra using the model from [94,95] is applicable for a time window from $\sim 2.5 \cdot 10^{-8}$ s to $\sim 10^{-10}$ s. In addition, Fig. 11 shows reference points corresponding to T_{max} in the $M(T)_{ZFC}$ dependences in a field of 100 Oe (Fig. 2). For these reference points, a value of $\tau = 10^2$ s was taken on the abscissa axis. It appeared that the data in Fig. 11 cannot be described within Néel expression (3), which does not take into account the IPI contribution.

In studying the τ(T) dependences of the systems of interacting particles, the scaling law is often used, which corresponds to a phase transition to the frozen state [105,109–111,61]. In this case, it is assumed that it is the IPI effect that causes the transition to the glass-like frozen state at the temperature T_g. The dynamic scaling law is written in the form

$$\tau = \tau^* \cdot (T/T_g - 1)^{-z}. \quad (7)$$

In Eq. (7), τ* is the relaxation time of noninteracting particles and the exponent z can change; for spin glasses, the range $4 \le z \le 12$ is usually indicated [105,109–111,61]. By analogy with spin glasses, the fulfillment of law (7) in the τ(T) dependence for nanoparticles is interpreted as a transition to the super-spin glass state at the temperature T_g. Here, the term super-spin is applied to the magnetic moment of a nanoparticle (in AFM nanoparticles, to the uncompensated magnetic moment μ_{un}).

In Fig. 11, solid lines showing the experimental τ(T) data illustrate the results of fitting by Eq. (7). The fitting parameters are shown in the legend. The τ* values are quite reasonable and the exponent z is at the edge of the above-mentioned range ($4 \le z \le 12$). At the same time, in Eq. (7), τ becomes equal to τ* at $T = 2T_g$, i.e., at T = 48 and 88 K. Further extrapolation of scaling dependence (7) to the higher-temperature

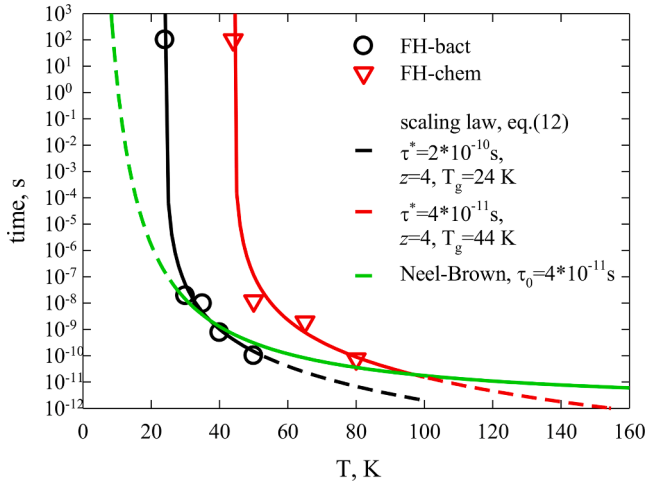

Fig. 11. Relaxation times (symbols) at different temperatures obtained by processing the Mössbauer spectra (Fig. 10) using the model from [94,95]. Points at an ordinate of 10^2 s corresponds to the T_{max} values from the magnetic measurements (Fig. 2). Lines are built according to scaling law (7) with the parameters indicated in the legend and Néel-Brown relation (3), see the text. The solid (dashed) lines show the temperature range of consistency (inconsistency) of the model dependences with the experimental data.

portion (larger than $2T_g$,) will no longer be reasonable, since the relaxation times will be nonphysically short. In the indicated temperature range, it is more correct to use Néel-Brown relation (3). Fig. 11 shows the τ(T) dependence built using Eq. (3). The K_{eff} value was taken to be $2.1 \cdot 10^6$ erg/cm^3 (see Section 4.2), $V = d^3 \cdot \pi/6$ at $d = d_{max} \approx 3.3$ nm (Section 3.1), and the τ_0 value was taken the same as at the estimated SPM blocking temperatures (10^{-12} s). Fig. 11 schematically shows that the Neel-Brown formula works in the region of sufficiently high temperatures. In the vicinity of $2T_g$, the onset of freezing of the magnetic moments under the action of the IPI contribution occurs and, then, with decreasing temperature, the relaxation time increases according to scaling law (7). In the investigated samples, the IPIs manifest themselves in different degrees: the larger T_g value corresponds to the stronger IPI effect in the chemical ferrihydrite sample. Certainly, in the high-temperature region, the IPI contribution is also preserved and affects the properties of an ensemble of particles; however, in the indicated range (below $\sim 2T_g$), this effect leads to an increase in the relaxation time.

The evidence obtained in Section 3.4 (Mössbauer spectroscopy) and Section 4.1 for the presence of the IPIs, which manifest themselves differently in the two examined samples, suggests that the IPIs are responsible for the observed differences in the behavior of the M(T) dependences (Section 3.2) and parameters of the FMR spectra (Section 3.3).

Effect of an external field on the transition to the SPM state (Magnetometry)

Based on the experimental data presented in Section 3, we can unambiguously determine the temperatures of the transition to the SPM state for only two techniques (magnetometry and Mössbauer spectroscopy). To better understand the origin of a frequency gap in the FMR field-frequency dependences and its temperature dependence (Section 3.4), we need to know in which (blocked or unblocked) state the magnetic moments of particles are under the magnetic resonance conditions. We, of course, can estimate the blocking temperature using Eq. (4) or (6) with the T_0 values obtained above by substituting the characteristic measurement time $\tau_m = 1/\nu$. However, the FMR is detected in a sufficiently strong external field (1–20 kOe). The field dependence of the temperature of the transition to the SPM state is determined by the fact that the external field reduces the energy barrier $E = K_{eff} \cdot V$, which is overcome by the magnetic moment of a particle: $E = K_{eff} \cdot V - \mu_{un} \cdot H$. Below, we consider the experimental $T_B(H)$ dependence established from the magnetic measurements for its further extrapolation to the FMR conditions.

Fig. 12 presents portions of the $M(T)_{ZFC}$ and $M(T)_{FC}$ dependences in fields of 1 and 10 kOe for the investigated samples. It is noteworthy that, for sample FH-chem in a field of 1 kOe, the behavior of the $M(T)_{ZFC}$ and $M(T)_{FC}$ dependences is extraordinary: the temperature T_{irr} of the irreversible behavior of the magnetization is lower than T_{max}. However, in fields of 1, 10, and 100 Oe and 10 and 30 kOe, we have $T_{irr} \ge T_{max}$. For sample FH-bact, it is always $T_{irr} \ge T_{max}$. Below, we operate with the T_{irr} values, assuming that, at this temperature, the transition of the largest particles to the SPM state occurs. The $T_{irr}(H)$ dependences are shown in Fig. 13 (symbols). It is noteworthy that, in relatively low fields, the T_{irr} values for the two samples are drastically different, while in strong fields (30 kOe) they are already similar.

For systems of noninteracting magnetic particles, the field dependence of the temperature of the transition to the SPM state is determined as [112,113]

$$T_B(H) = \frac{K_{eff} V}{k_B ln(\tau m/\tau_0)} \left[1 - \frac{M_S H}{2K_{eff}}\right]^{3/2}. \quad (8)$$

Here, M_S is the saturation magnetization. In the case of interacting particles, the modified random anisotropy model (RAM) developed in

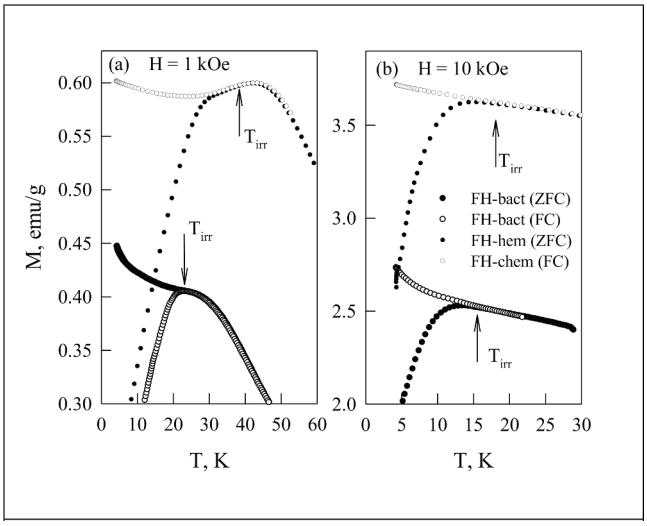

Fig. 12. Portions of the $M(T)_{ZFC}$ and $M(T)_{FC}$ dependences for the samples under study in fields of H = (a) 1 and (b) 10 kOe illustrating the presence of temperature T_{irr} of the irreversible magnetization behavior. The legend in (b) corresponds to both figures.

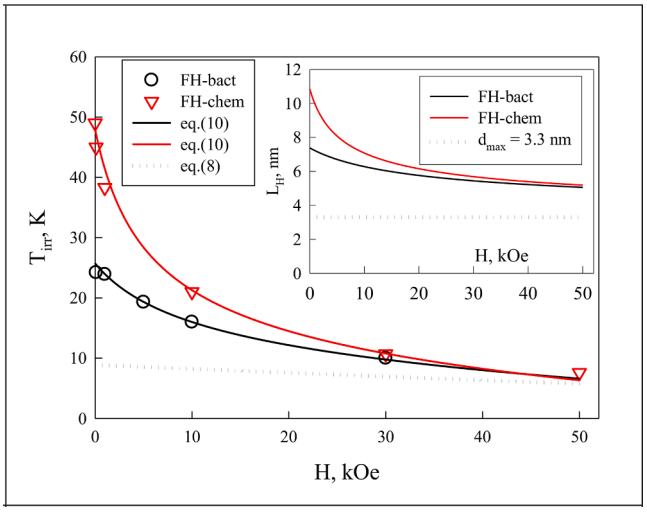

Fig. 13. Dependences of temperature T_{irr} of the irreversible magnetization behavior on external field H obtained from the $M(T)_{ZFC}$ and $M(T)_{FC}$ data for the samples under study (symbols). Solid lines are plotted using Eq. (10) of the RAM model [112,113] and a dotted line, using Eq. (8), see the text. Inset: $L_H(H)$ dependences (Eq. (9)) used in fitting of $T_{irr}(H)$ dependences by Eq. (10).

[112,113] is used. Instead of an isolated particle, this model considers a coarser cluster, which includes a certain number of particles, depending on volume concentration x. The correlation length L_H of such a cluster is related to the external field as

$$L_H = d + \sqrt{\frac{2A_{eff}}{M_S H + C}} \tag{9}$$

Here, both parameters, A_{eff} and C, correspond to the IPI intensity. For a cluster of correlation length L_H consisting of N particles, the anisotropy constant also changes as

$$Keff \rightarrow \frac{Keff}{\sqrt{N}} = \frac{Keff}{\sqrt{1+\frac{x(L_H^3-d^3)}{d^3}}}$$

As a result, the $T_B(H)$ dependence (Eq. (8)) is transformed to

$$T_B(H) = \frac{\pi K_{eff}\left[d^3 + x(L_H^3 - d^3)\right]}{6k_B ln\left(\frac{\tau_m}{\tau_0}\right)\sqrt{1+\frac{x(L_H^3-d^3)}{d^3}}} \times \left[1 - \frac{HM_S\sqrt{1+\frac{x(L_H^3-d^3)}{d^3}}}{2K_{eff}}\right]^{\frac{3}{2}} \tag{10}$$

First of all, we note that we failed to achieve the agreement with the experimental T_{irr} values using Eq. (8); a typical example of the fitting is shown in Fig. 13 (dotted curve). When processing the data by Eq. (10), we made the following assumptions to decrease the number of variable parameters. The K_{eff} values and $d = d_{max} = 3.3$ nm were the same due to the identity of the particle sizes. The times τ_m and τ_0 were taken to be 10^2 s and 10^{-12} s, respectively. The M_S value was also taken to be the same for both samples (5 emu/g, according to Fig. 4b); the change in this value within 20% weakly affected the results. The concentration is $\times$ = 1 for sample FH-chem and $\times$ = 0.65 for sample FH-bact (this quantity can be determined under the reasonable assumption that particles are coated with a 0.5-nm-thick shell). In fact, to describe the experimental $T_B(H)$ dependence, we have to choose the field dependence of the correlation length L_H (Eq. (9)). An increase in the parameter A_{eff} and, consequently, a decrease in the parameter C imply the stronger IPI effect [112,113]. The good fitting results for sample FH-bact are obtained at the C and A_{eff} values ranging within $2.1–1.1 \cdot 10^4$ erg/cm^3 and $1–2 \cdot 10^{-8}$ erg/cm, respectively. For sample FH-chem, the ranges of these parameters are narrower: the parameter C can be $0.75–0.95 \cdot 10^4$ erg/cm^3 and A_{eff} can change within $1.8–2.2 \cdot 10^{-8}$ erg/cm. To describe the experience, we took $C = 1.1 \cdot 10^4$ erg/cm^3 and $A_{eff} = 1.5 \cdot 10^{-8}$ erg/cm for sample FH-bact and $C = 0.85 \cdot 10^4$ erg/cm^3 and $A_{eff} = 2.0 \cdot 10^{-8}$ erg/cm for sample FH-chem.

The fitting results are shown in Fig. 13 by solid lines. We can state that the calculated values are in good agreement with the experimental data. The behavior of the parameter L_H of the two samples is presented in the inset to Fig. 13, which, for comparison, shows also the size d_{max} (dotted line). It can be seen that, in the region of the relatively low fields, L_H multiply exceeds d_{max}, and, for sample FH-chem, it is higher than for sample FH-bact. The larger correlation length, i.e., the characteristic size where the magnetic moments of particles behave consistently evidences for the IPI effect.

The results were obtained at $K_{eff} = 2.1 \cdot 10^6$ erg/cm^3 (the same for particles of both samples). This method for determining the effective constant of the magnetic anisotropy (in the framework of the RAM) is apparently more justified than the use of Eq. (6), i.e., the Vogel-Fulcher law. At the T_0 values specified in Section 4.1, the K_{eff} values of the samples under study appeared different ($2.5 \cdot 10^6$ and $2.0 \cdot 10^6$ erg/cm^3 for FH-bact and FH-chem, respectively). The K_{eff} value obtained in the RAM approach does not include the IPI contribution introduced in Vogel-Fulcher law (6) as T_0. A value of $2.1 \cdot 10^6$ erg/cm^3 significantly exceeds typical bulk magnetic anisotropy constants of magnetically ordered oxides [15,16,47], which is unambiguously interpreted as a contribution of the surface magnetic anisotropy [45–48].

Line of the transition to the SPM state in the H–T diagram under the FMR conditions

The $T_{irr}(H)$ dependences obtained by processing of the experiment (Eq. (10), Fig. 13) were used for scaling to the FMR conditions. In Eq. (10), we used $\tau_m = 1/\nu$. These dependences, including the $T_{irr}(H)$ dependence from the magnetic measurements, are presented in Fig. 14 in the coordinates (H, T). The lines shown in the legend as (T_B-H) separate the SPM (on the right) and blocked (on the left) states. In addition, Fig. 14 shows temperature dependences of the resonance fields at different FMR frequencies and indicates the temperatures T* at which the gap opens (the beginning of the deviation of the $H_R(T)$ dependence from a constant value). We can state that, as the temperature decreases, in both samples at frequencies of 25–75 GHz first the transition to the

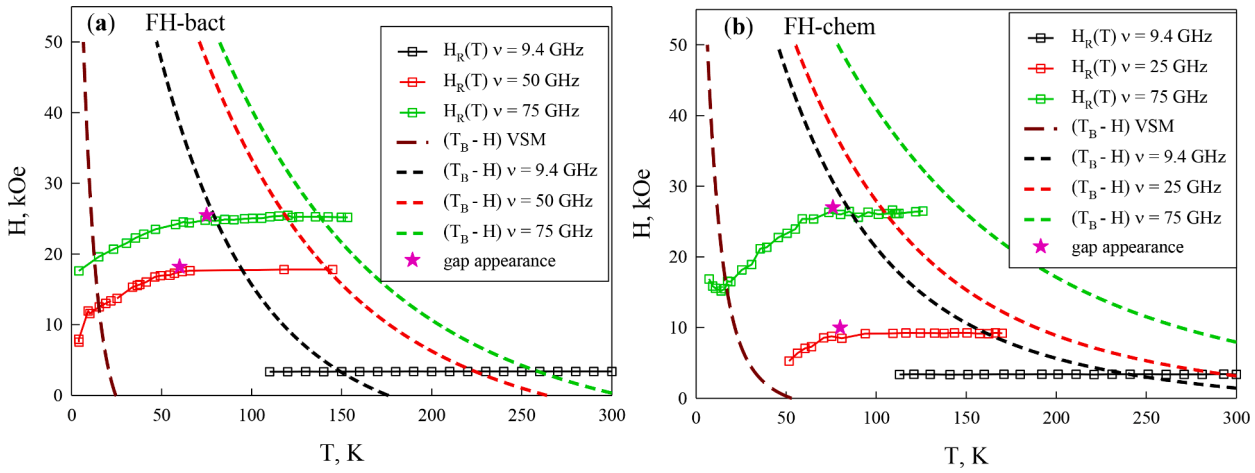

Fig. 14. Lines T_B-H separating the blocked (to the left of the line) and SPM (to the right of the line) states in the coordinates (H, T) for the static (VSM) magnetometry and FMR techniques at the indicated frequencies. In addition, the dependences of the resonant field at the indicated frequencies are shown. The asterisk marks the beginning of the deviation of H_R from a constant value with decreasing temperature. Data for samples (a) FH-bact and (b) FH-chem.

blocked state (at the point of intersection of the dependence $H_R(T)$ = const with the T_B-H line) occurs and then, at lower temperatures, the gap opens (the induced anisotropy arises).

It can be seen in Fig. 14 that, in the measurements at a frequency of 9.4 GHz, the transition from the blocked to SPM state occurs at temperatures of T ~ 150 and ~ 250 K for samples FH-bact and FH-chem, respectively. This corresponds to the beginning of the temperature range in which the integral intensity obeys the law $I(T) \sim 1/T + \text{const}$ (Sec. 3.3.1, Fig. 6b). Hence, according to the FMR data, the transition to the SPM state can be established from the behavior of the integral intensity.

Induced anisotropy and behavior of the FMR parameters

The occurrence of the induced anisotropy at the temperature T*, which is much lower than the SPM particle blocking temperature, can be explained by the freezing of the surface spin subsystem and establishment of an exchange coupling between this subsystem and the core. This phenomenon is well-known and was observed in different systems of magnetic nanoparticles using different techniques [51–54]; as a rule, $T^* < T_B$. The T* value should depend not only on the characteristic measurement time, but also on the external field and, apparently for this reason, an obvious trend of the change of the T* value from $\tau_m = 1/\nu$ was not found (Fig. 14). It is clear that, in the static magnetic measurements, the T* values should be lower than under the FMR conditions; i.e., $T^*_{Magn} < T^*_{FMR}$. Thus, the gap in the field-frequency dependences $\nu(H)$ in Fig. 8 can be considered to be a surface effect related to the exchange coupling of the subsystem of surface spins with a particles core.

The T* values for the two investigated samples are similar. Therefore, the IPIs do not affect the temperature at which the surface-core exchange coupling arises. However, at low temperatures, there is a difference in the behavior of the $H_R(T)$ dependences (see Figs. 9 and 14). Let us consider in more detail the behavior of parameters of the FMR spectra (linewidth ΔH and integral intensity I) at frequencies of 25–75 GHz. We denote the induced anisotropy field as $H^A = H_{RS} - H_R$ (H_{RS} is the resonance field at which $H_R(T) \approx$ const at sufficiently high temperatures). The $H^A(T)$, ΔH(T), and I(T) dependences are presented in Fig. 15. For sample FH-bact (Fig. 15a), these dependences monotonically increase with decreasing temperature. A different picture is observed for sample FH-chem (Fig. 15b): all the investigated parameters behave nonmonotonically.

The exchange coupling of the subsystem of surface spins with the core within one particle, can be compared with the AFM/FM bilayers (FM is a ferromagnet) [114,115]. In this case, we identify the particle

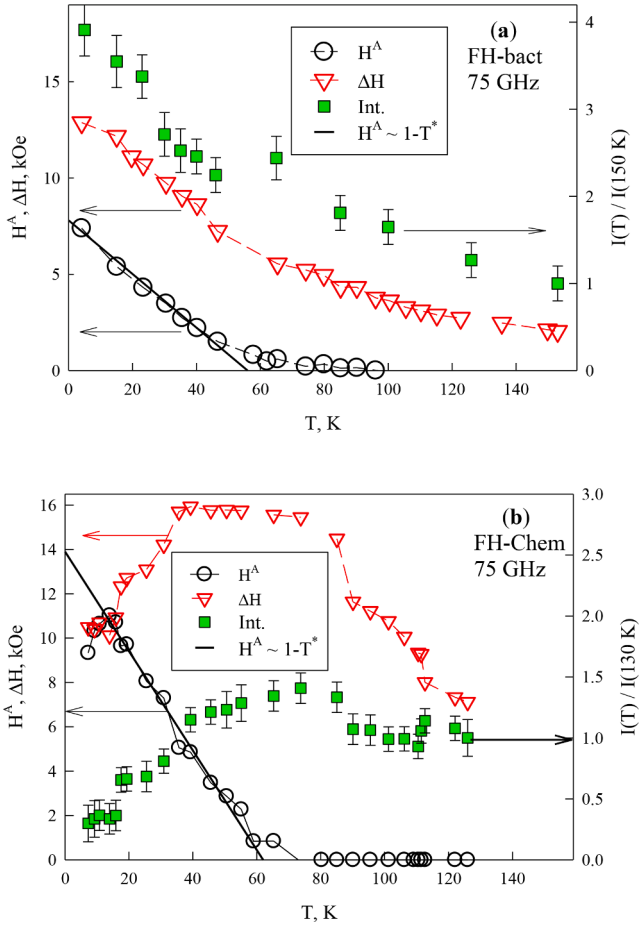

Fig. 15. Parameters (induced anisotropy field $H^A = H_{RS} - H_R$, linewidth ΔH, and normalized integral intensity I) of the FMR spectra for samples (a) FH-bact and (b) FH-chem as functions of temperature. Straights correspond to the $H^A(T)$ dependence according to Eq. (11).

core with the uncompensated moment μ_{un} to a FM and the subsystem of surface spins (in the frozen state), to an AFM spacer. In AFM/FM systems, the unidirectional exchange anisotropy increases with a decrase in temperature and the corresponding $H^A(T)$ dependence is determined by a type of the magnetic anisotropy in the layer in which the exchange spin

spring is formed [116]. For the uniaxial anisotropy, the law $H^A(T) \sim (1–T/T^*)^{1.5}$ is met; for the cubic anisotropy, there is a linear dependence [116] of the anisotropy field:

$$H^A(T) \sim (1–T/T^*). \quad (11)$$

In our case, the pinning layer is a shell in the spin glass state. Here, the uniaxial anisotropy is improbable, so it is quite reasonable to assume that law (11) works. Taking into account the spread of the particle sizes, we can expect a monotonic increase in H^A with decreasing temperature, rather than the strict validity of dependence (11). Nevertheless, the data for sample FH-bact at temperatures from 4 to 50 K are satisfactorily described by dependence (11) at the T* value somewhat lower than the temperature at which the trend $H^A \rightarrow 0$ is experimentally observed (Fig. 15a). For sample FH-chem, the $H^A(T)$ behavior can also be satisfactorily described by Eq. (11), except, however, for the region $T < 15$ K (Fig. 15b).

In [117], basing on the phenomenological analysis, the relation between the absorption linewidth ΔH and the resonance field *change* (in our notation, H^A) was obtained According to the results of this work, we have

$$H^A \sim (\Delta H)^m, \quad (12)$$

where $m = 2$ for partially oriented particles and $m = 3$ for randomly misoriented particles. Relation (12) was experimentally confirmed in several studies on the FM [52,74,75,82] and AFM [83] nanoparticle samples. Fig. 16 shows the experimental H^A vs ΔH data for the investigated ferrihydrite samples in double logarithmic coordinates. It can be seen that the data on sample FH-bact follow relation (12) with good accuracy at $m = 3$ (the straight in Fig. 16). It can be concluded that the monotonic increase in the linewidth with decreasing temperature correlates with an increase in H^A, which is explained in the phenomenological FMR consideration.

For sample FH-chem, relation (12) is not met (Fig. 16), which, at first glance, is no surprise. For sample FH-bact, the ΔH value changes several times below T* (Fig. 15a), while for sample FH-chem, ΔH(T) is a non-monotonic function in this temperature range (Fig. 15b). At 35–85 K, the linewidth remains almost unchanged upon temperature variation and, below 35 K, it decreases. The intensity of the absorption line also decreases at temperatures below 80 K, which cannot be attributed to the SPM blocking, as was shown in Section 4.3 (Fig. 14b). Therefore, one should look for other causes for the observed behavior.

As shown in Section 4.1, the IPIs lead to the collective effect of increasing the particle relaxation time (Fig. 11) in the temperature region below $\sim 2T_g$ ($T_g \approx 44$ K for sample FH-chem). This should affect the behavior of the FMR parameters, although it must be taken into account that the external field is strong and the magnetic moments of particles in it are directed mainly along the external field. To have a resonant response, the magnetic moments should precess at a microwave frequency. Obviously, in addition to the effects caused by the magnetic anisotropy of the particles themselves, the resonance response should also be affected by the particle relaxation time τ. Certainly, τ is the characteristic time of reversal of the magnetic moment μ_{un}; however, if the moments are already oriented mainly along the field direction, the large time τ should influence also the possibility of the magnetic moment precession. Then, for a part of the magnetic moments of particles, the resonance condition will no longer be met, so the integral intensity should decrease with temperature. This can be seen from the experimental data for sample FH-chem in Fig. 15b. A decrease in the linewidth below 40 K can be attributed to the fact that, with decreasing temperature, the fraction of resonating particles, which had the larger ΔH value at high temperatures, decreases. A similar behavior was observed in [83] at a frequency of 190 GHz for chemical ferrihydrite, although the behavior (the presence of the ΔH maximum or its weak temperature dependence) depended on the microwave radiation frequency.

Concerning sample FH-bact, the processes of increase of the relaxation (freezing) time of the magnetic moments in it occur at lower temperatures comparing with FH-chem sample (Fig. 11). In this case, apparently due to the weaker impact of the IPI, the behavior of the resonance parameters can be adequately explained based on the general concepts (Fig. 16). It is noteworthy that there is one more characteristic time in the FMR detection technique used: the pulse length (~12 ms). Although this time is larger than the inverse microwave radiation frequency by several orders of magnitude, at a rapid change in the external field, the shape of the magnetization curve can also change (not all particle magnetic moments have time to orient along the field) relative to the static changes in the magnetization [48,118,119].

The presence of the $H_R(T)$ minimum around 15 K (Fig. 14b) and, consequently, the $H_A(T)$ maximum at this temperature (Fig. 15b) for sample FH-chem cannot be easily interpreted. This feature may be related to the long relaxation time of the particle magnetic moments at low temperatures; in addition, in the pulsed technique, the effect of "lagging" in the magnetic moment orientation along the field is superimposed.

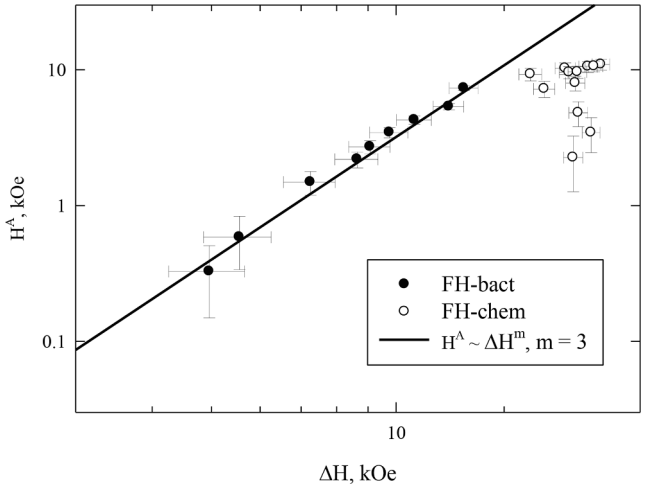

Fig. 16. Induced anisotropy field H^A ($H^A = H_{RS} – H_R$) vs ΔH for the data in Fig. 15 in a double logarithmic scale. The solid line corresponds to the exponent $m = 3$ of Eq. (12).

Concluding remarks

The investigated powder systems of biogenic and chemical ferrihydrite are characterized by the close nanoparticle size distributions, similar magnetic characteristics (magnetization and uncompensated magnetic moment) of individual particles and, at the same time, different degrees of the IPI effect. In the static magnetic properties (the M(T) dependences), the IPI manifest themselves as an increase in the temperature of the transition to the SPM state, a deviation of the M(T) dependence from the function ~ 1/T in the SPM state, and a higher coercivity in the blocked state (at $T = 4.2$ K). An increase in the temperature of the transition to the SPM state is confirmed also by a technique with a much shorter characteristic measurement time τ_m: Mössbauer spectroscopy. In the temperature region of the transition from the SPM to blocked state, a relaxation component appears in the Mössbauer spectra, which is indicative of the IPI effect. The account for this component in the model from [93,94] made it possible to determine the particle relaxation time. The resulting τ(T) dependences obey the scaling law $\tau = \tau^* \cdot (T/T_g – 1)^{-z}$ with the exponent $z = 4$, which suggests the collective freezing of the magnetic moments of particles and the transition to the so-called super-spin glass state. The temperature T_g for the powder chemical ferrihydrite system (44 K) is almost two times as high as T_g of the similar biogenic ferrihydrite system (24 K). The study of the field dependence of the temperature of the transition to the SPM

state by the static magnetic measurements and its scaling to the FMR characteristic times allowed us to establish the temperature limits of the SPM and blocked states in which the particle magnetic moments lie under the FMR conditions at the microwave frequencies used (9.4, 25, 50, and 75 GHz).

The above-described analysis made it possible to interpret a set of FMR data obtained in the specified frequency band and a wide temperature range as follows. The IPIs lead to an increase in the linewidth both in the SPM and blocked state. In addition, as in other techniques, the IPIs manifest themselves in the higher temperature of the transition to the SPM state. In the SPM state, the integral FMR intensity, as a rule, decreases with increasing temperature according to the law $I \sim 1/T +$ const. At low temperatures, the field-frequency dependences $\nu(H)$ contain a gap of about 10 kOe caused by the induced anisotropy H^A. A decrease in the gap with increasing temperature is approximately linear and, at temperatures of 60–80 K, we have $H^A \rightarrow 0$. This behavior was observed for both investigated samples, which are obviously in the blocked state in this temperature range. Therefore, the presence of a gap (the induced anisotropy) is an intrinsic property of ferrihydrite particles and the IPIs are not a factor determining it. The most reasonable explanation for the induced anisotropy is the exchange coupling between the frozen subsystem of surface spins and the uncompensated moment of a particle.

The strong impact of the IPIs leading to the collective freezing of the magnetic moments of particles and the transition to the super-spin glass state manifests itself in the chemical ferrihydrite sample in the non-monotonic behavior of the FMR linewidth and integral intensity in the low-temperature region (below 80 K, i.e., around $2T_g$). This is most likely due to the increasing particle relaxation time, starting with a temperature of about $2T_g$. Indeed, the large τ value should affect the possibility of the magnetic moment precession; as a result, some magnetic moments will not be able to precess at the microwave radiation frequency. As the temperature decreases, the fraction of particles (or, to be exact, the magnetic moments of particles) involved in the resonant precession decreases. At the same time, for the biogenic ferrihydrite sample, in which the IPI effect is weaker and the collective effects only take place at sufficiently low temperatures, the canonical (standard) relation $H^A = H_R - H_{RS} \sim (\Delta H)^3$ [117] between the linewidth and resonance field is satisfied.

CRediT authorship contribution statement

D.A. Balaev: Conceptualization, Investigation, Data curation, Funding acquisition, Visualization, Writing – original draft, Methodology, Software, Writing – review & editing. **S.V. Stolyar:** Investigation, Data curation. **Yu.V. Knyazev:** Writing – original draft, Data curation, Formal analysis, Investigation, Visualization, Writing – review & editing, Funding acquisition. **R.N. Yaroslavtsev:** Investigation, Visualization. **A.I. Pankrats:** Investigation, Data curation, Validation. **A.M. Vorotynov:** Investigation, Visualization. **A.A. Krasikov:** Investigation, Data curation. **D.A. Velikanov:** Investigation, Software. **O.A. Bayukov:** Validation, Software, Formal analysis, Investigation, Software. **V.P. Ladygina:** Investigation, Software. **R.S. Iskhakov:** Supervision.

Declaration of Competing Interest

The authors declare that they have no known competing financial interests or personal relationships that could have appeared to influence the work reported in this paper.

Acknowledgments

Authors thank to A.D. Balaev, S.V. Komogortsev for fruitful discussions and M.N. Volochaev for TEM studies. The TEM study and measurements of X-band FMR spectra were carried out on the equipment of the Krasnoyarsk Territorial Center for Collective Use, Krasnoyarsk Scientific Center, Siberian Branch, Russian Academy of Sciences.

Funding

This study was supported by the Russian Science Foundation, project no. 21-72-00025 (https://rscf.ru/project/21-72-00025/) “Tuning the Magnetic Properties of Ultrafine Biocompatible Ferrihydrite Nanoparticles through Interparticle Interactions”.

References

[1] Ashour AH, El-Batal AI, Maksoud MIAA, El-Sayyad GS, Labib Sh, Abdeltwab E, et al. Antimicrobial activity of metal-substituted cobalt ferrite nanoparticles synthesized by sol–gel technique. Particuology 2018;40:141–51. https://doi.org/10.1016/j.partic.2017.12.001.

[2] Amiri S, Shokrollahi H. The role of cobalt ferrite magnetic nanoparticles in medical science. Mater Sci Eng, C 2013;33:1–8. https://doi.org/10.1016/j.msec.2012.09.003.

[3] Yadavalli T, Jain H, Chandrasekharan G, Chennakesavulu R. Magnetic hyperthermia heating of cobalt ferrite nanoparticles prepared by low temperature ferrous sulfate based method. AIP Adv 2016;6:055904. https://doi.org/10.1063/1.4942951.

[4] Roca AG, Gutiérrez L, Gavilán H, Fortes Brollo ME, Veintemillas-Verdaguer S, del Puerto Morales M. Design strategies for shape-controlled magnetic iron oxide nanoparticles. Adv. Drug. Deliver. Rev. 2019;138:68–104. https://doi.org/10.1016/j.addr.2018.12.008.

[5] Khanna L, Verma NK, Tripathi SK. Burgeoning tool of biomedical applications-superparamagnetic nanoparticles. J Alloy Compd 2018;752:332–53. https://doi.org/10.1016/j.jallcom.2018.04.093.

[6] Mohapatra M, Hariprasad D, Mohapatra L, Anand S, Mishra B. Mg-doped nano ferrihydrite—a new adsorbent for fluoride removal from aqueous solutions. Appl Surf Sci 2012;258(10):4228–36. https://doi.org/10.1016/j.apsusc.2011.12.047.

[7] Kocar BD, Borch T, Fendorf S. Arsenic repartitioning during biogenic sulfidization and transformation of ferrihydrite. Geochem Cosmochim Acta 2010;74(3):980–94. https://doi.org/10.1016/j.gca.2009.10.023.

[8] Singamaneni S, Bliznyuk VN, Binek C, Tsymbal EY. Magnetic nanoparticles: recent advances in synthesis, self-assembly and applications. J Mater Chem 2011;21:16819. https://doi.org/10.1039/C1JM11845E.

[9] Kefeni KK, Msagati TAM, Mamba BB. Ferrite nanoparticles: synthesis, characterisation and applications in electronic device. Mater. Sci. Eng., B 2017;215:37–55. https://doi.org/10.1016/j.mseb.2016.11.002.

[10] Ohkoshi S, Namai A, Yoshikiyo M, Imoto K, Tamazaki K, Matsuno K, et al. Multimetal-substituted epsilon-iron oxide ϵ-$Ga_{0.31}Ti_{0.05}Co_{0.05}Fe_{1.59}O_3$ for next-generation magnetic recording tape in the big-data era. Angew Chem 2016;128:11575. https://doi.org/10.1002/ange.201604647.

[11] Zhang Q, Yang X, Guan J. Applications of magnetic nanomaterials in heterogeneous catalysis ACS Appl. Nano Mater 2019;2(8):4681–97. https://doi.org/10.1021/acsanm.9b00976.

[12] Nowitzki T, Carlsson AF, Martyanov O, Naschitzki M, Zielasek V, Risse T, et al. Oxidation of alumina-supported Co and Co–Pd model catalysts for the Fischer−Tropsch reaction. J Phys Chem C 2007;111(24):8566–72. https://doi.org/10.1021/jp066796r.

[13] Bukhtiyarova GA, Delii IV, Sakaeva NS, Kaichev VV, Plyasova LM, Bukhtiyarov VI. Effect of the calcination temperature on the properties of Fe_2O_3/SiO_2 catalysts for oxidation of hydrogen sulfide. React Kinet Catal Lett 2007;92:89. https://doi.org/10.1007/s11144-007-5177-2.

[14] Yakushkin SS, Bukhtiyarova GA, Dubrovskiy AA, Knyazev YV, Balaev DA, Martyanov ON. In situ FMR study of the selective H_2S-oxidation stability of ε-Fe_2O_3/SiO_2 catalysts. Appl Magn Reson 2019;50(5):725–33. https://doi.org/10.1007/s00723-019-1109-3.

[15] Sangaiya P, Jayaprakash R. A review on iron oxide nanoparticles and their biomedical applications. J Supercond Nov Magn 2018;31(11):3397–413. https://doi.org/10.1007/s10948-018-4841-2.

[16] Narang SB, Pubby K. Nickel spinel ferrites: a review. J Magn Magn Mater 2021;519:167163. https://doi.org/10.1016/j.jmmm.2020.167163.

[17] Seehra MS, Babu VS, Manivannan A, Lynn JW. Neutron scattering and magnetic studies of ferrihydrite nanoparticles. Phys Rev B 2000;61:3513. https://doi.org/10.1103/PhysRevB.61.3513.

[18] Néel L. Superparamagnétisme des grains très fins antiferromagnétiques. CR Acad Sci Paris 1961;252:4075.

[19] Makhlouf SA, Parker FT, Berkowitz AE. Magnetic hysteresis anomalies in ferritin. Phys Rev B 1997;55:R14717. https://doi.org/10.1103/PhysRevB.55.R14717.

[20] Gilles C, Bonville P, Wong KKW, Mann S. Non-Langevin behaviour of the uncompensated magnetization in nanoparticles of artificial ferritin. Eur Phys J B 2000;17:417. https://doi.org/10.1007/s100510070121.

[21] Gilles C, Bonville P, Rakoto H, Broto JM, Wong KKW, Mann S. Magnetic hysteresis and superantiferromagnetism in ferritin nanoparticles. J Magn Magn Mater 2002;241:430. https://doi.org/10.1016/S0304-8853(01)00461-9.

[22] Punnoose A, Phanthavady T, Seehra M, Shah N, Huffman G. Magnetic properties of ferrihydrite nanoparticles doped with Ni, Mo, and Ir. Phys Rev B 2004;69(5):054425. https://doi.org/10.1103/PhysRevB.69.054425.

[23] Silva NJO, Amaral VS, Carlos LD. Relevance of magnetic moment distribution and scaling law methods to study the magnetic behavior of antiferromagnetic

nanoparticles: application to ferritin. Phys Rev B 2005;71:184408. https://doi.org/10.1103/PhysRevB.71.184408.
[24] Bahl CRH, Hansen MF, Pedersen T, Saadi S, Nielsen KH, Lebech B, et al. The magnetic moment of NiO nanoparticles determined by Mössbauer spectroscopy. J Phys: Condens Matter 2006;18(17):4161–75. https://doi.org/10.1088/0953-8984/18/17/005.
[25] Seehra MS, Singh V, Song X, Bali S, Eyring EM. Synthesis, structure and magnetic properties of non-crystalline ferrihydrite nanoflakes. J Phys Chem Solids 2010;71:1362–6. https://doi.org/10.1016/j.jpcs.2010.06.003.
[26] Tiwari SD, Rajeev KP. Effect of distributed particle magnetic moments on the magnetization of NiO nanoparticles. Solid State Commun 2012;152:1080. https://doi.org/10.1016/j.ssc.2012.03.003.
[27] Balaev DA, Dubrovskii A, Krasikov A, Stolyar SV, Iskhakov RS, Ladygina VP, et al. Mechanism of the formation of an uncompensated magnetic moment in bacterial ferrihydrite nanoparticles. JETP Lett 2013;98(3):139–42. https://doi.org/10.1134/S0021364013160029.
[28] Balaev DA, Krasikov AA, Dubrovskiy AA, Popkov SI, Stolyar SV, Bayukov OA, et al. Magnetic properties of heat treated bacterial ferrihydrite nanoparticles. J Magn Magn Mater 2016;410:71. https://doi.org/10.1016/j.jmmm.2016.02.059.
[29] Rani Ch, Tiwari SD. Superparamagnetic behavior of antiferromagnetic six lines ferrihydrite nanoparticles. Phys B 2017;513:58. https://doi.org/10.1016/j.physb.2017.02.036.
[30] Popkov SI, Krasikov AA, Dubrovskiy AA, Volochaev MN, Kirillov VL, Martyanov ON, et al. Size effects in the formation of an uncompensated ferromagnetic moment in NiO nanoparticles. J Appl Phys 2019;126:103904. https://doi.org/10.1063/1.5109054.
[31] Popkov SI, Krasikov AA, Velikanov DA, Kirillov VL, Martyanov ON, Balaev DA. Formation of the magnetic subsystems in antiferromagnetic NiO nanoparticles using the data of magnetic measurements in fields up to 250 kOe. J Magn Magn Mater 2019;483:21. https://doi.org/10.1016/j.jmmm.2019.03.004.
[32] Parmar C, Parmar GS. Structural and magnetic properties of six-line ferrihydrite nanoparticles. J Supercond Nov Magn 2020;33:441–4. https://doi.org/10.1007/s10948-019-05200-x.
[33] Iimor T, Imamoto Y, Uchida N, Kikuchi Y, Honda K, Iwahashi T, et al. Magnetic moment distribution in nanosized antiferromagnetic NiO. J Appl Phys 2020;127:023902. https://doi.org/10.1063/1.5135335.
[34] Balaev DA, Krasikov AA, Popkov SI, Semenov SV, Volochaev MN, Velikanov DA, et al. Uncompensated magnetic moment and surface and size effects in few-nanometer antiferromagnetic NiO particles. J Magn Magn Mater 2021;539:168343. https://doi.org/10.1016/j.jmmm.2021.168343.
[35] Tadić M, Panjan M, Marković D. NiO/SiO_2 nanostructure and the magnetic moment of NiO nanoparticles. Mater Lett 2010;64(19):2129–31. https://doi.org/10.1016/j.matlet.2010.07.006.
[36] Nikolić D, Panjan M, Blake GR, Tadić M. Annealing-dependent structural and magnetic properties of nickel oxide (NiO) nanoparticles in a silica matrix. J Eur Ceram Soc 2015;35(14):3843–52. https://doi.org/10.1016/j.jeurceramsoc.2015.06.024.
[37] Balaev DA, Krasikov AA, Stolyar SV, Iskhakov RS, Ladygina VP, Yaroslavtsev RN, et al. Change in the magnetic properties of nanoferrihydrite with an increase in the volume of nanoparticles during low-temperature annealing. Phys Solid State 2016;58:1782. https://doi.org/10.1134/S1063783416090092.
[38] Seehra MS, Punnoose A. Particle size dependence of exchange-bias and coercivity in CuO nanoparticles. Solid State Commun 2003;128(8):299–302. https://doi.org/10.1016/j.ssc.2003.08.029.
[39] Baran S, Hoser A, Penc B, Szytuła A. Size effects in antiferromagnetic NiO nanoparticles. Acta Phys Pol A 2016;129(1):35–9.
[40] Tadic M, Nikolic D, Panjan M, Blake GR. Magnetic properties of NiO (nickel oxide) nanoparticles: blocking temperature and Neel temperature. J Alloy Compd 2015;647:1061. https://doi.org/10.1016/j.jallcom.2015.06.027.
[41] Stolyar SV, Balaev DA, Ladygina VP, Dubrovskiy AA, Krasikov AA, Popkov SI, et al. Bacterial ferrihydrite nanoparticles: preparation, magnetic properties, and application in medicine. J Supercond Nov Magn 2018;31(8):2297–304. https://doi.org/10.1007/s10948-018-4700-1.
[42] Inzhevatkin EV, Kolenchukova OA, Dobretsov KG, Ladygina VP, Boldyreva AV, Stolyar SV. Efficiency of ampicillin-associated biogenic ferrihydrite nanoparticles in combination with a magnetic field for local treatment of burns. Bull Exp Biol Med 2020;169:683–6. https://doi.org/10.1007/s10517-020-04954-y.
[43] Stolyar SV, Ladygina VP, Boldyreva AV, Kolenchukova OA, Vorotynov AM, Bairmani MS, et al. Synthesis, properties, and in vivo testing of biogenic ferrihydrite nanoparticles. Bull Russ Acad Sci Phys 2020;84(11):1366–9. https://doi.org/10.3103/S106287382011026X.
[44] Stolyar SV, Kolenchukova OA, Boldyreva AV, Kudryasheva NS, Gerasimova YV, Krasikov AA, et al. Biogenic ferrihydrite nanoparticles: synthesis, properties in vitro and in vivo testing and the concentration effect. Biomedicines 2021;9:323. https://doi.org/10.3390/biomedicines9030323.
[45] Aharoni A. Surface anisotropy in micromagnetics. J Appl Phys 1987;61(8):3302–4. https://doi.org/10.1063/1.338890.
[46] Bødker F, Mørup S, Linderoth S. Surface effects in metallic iron nanoparticles. Phys Rev Lett 1994;72:282. https://doi.org/10.1103/PhysRevLett.72.282.
[47] J. Mohapatra, M. Xing, J. Elkins, J. Beatty, J Ping Liu, J. Phys. D: Appl. Phys. 53, 504004 (2020).
[48] Balaev DA, Poperechny IS, Krasikov AA, Semenov SV, Popkov SI, Knyazev YV, et al. Dynamic remagnetisation of $CoFe_2O_4$ nanoparticles: thermal fluctuational thawing of anisotropy. J Phys D Appl Phys 2021;54:275003. https://doi.org/10.1088/1361-6463/abf371.
[49] Kodama RH, Berkowitz AE, McNiff EJ, Foner S. Surface spin disorder in ferrite nanoparticles. J Appl Phys 1997;81:5552. https://doi.org/10.1063/1.364659.
[50] Kodama RH, Berkowitz AE. Atomic-scale magnetic modeling of oxide nanoparticles. Phys Rev B 1999;59:6321. https://doi.org/10.1103/PhysRevB.59.6321.
[51] Martínez B, Obradors X, Balcells Ll, Rouanet A, Monty C. Low temperature surface spin-glass transition in γ-Fe_2O_3 nanoparticles. Phys Rev Lett 1998;80:181–4. https://doi.org/10.1103/PhysRevLett.80.181.
[52] Koksharov YA, Gubin SP, Kosobudsky ID, Yurkov GY, Pankratov DA, Ponomarenko LA, et al. Electron paramagnetic resonance spectra near the spin-glass transition in iron oxide nanoparticles. Phys Rev B 2000;63:012407. https://doi.org/10.1103/PhysRevB.63.012407.
[53] Winkler E, Zysler RD, Vasquez Mansilla M, Fiorani D. Surface anisotropy effects in NiO nanoparticles. Phys Rev B 2005;72:132409. https://doi.org/10.1103/PhysRevB.72.132409.
[54] Winkler E, Zysler RD, Vasquez Mansilla M, Fiorani D, Rinaldi D, Vasilakaki M, et al. Surface spin-glass freezing in interacting core–shell NiO nanoparticles. Nanotechnol 2008;19:185702. https://doi.org/10.1088/0957-4484/19/18/185702.
[55] Khurshid H, Lampen-Kelley P, Iglesias Ò, Alonso J, Phan M-H, Sun C-J, et al. Spin-glass-like freezing of inner and outer surface layers in hollow γ-Fe_2O_3 nanoparticles. Sci Rep 2015;5:15054. https://doi.org/10.1038/srep15054.
[56] Rinaldi-Montes N, Gorria P, Martínez-Blanco D, Fuertes AB, Fernández Barquín L, Puente-Orench I, et al. Scrutinizing the role of size reduction on the exchange bias and dynamic magnetic behavior in NiO nanoparticles. Nanotechnol 2015;26:305705. https://doi.org/10.1088/0957-4484/26/30/305705.
[57] Tadic M, Panjan M, Marković D, Milošević I, Spasojević V. Unusual magnetic properties of NiO nanoparticles embedded in a silica matrix. J Alloy Compd 2011;509:7134. https://doi.org/10.1016/j.jallcom.2011.04.032.
[58] Stolyar SV, Balaev DA, Ladygina VP, Pankrats AI, Yaroslavtsev RN, Velikanov DA, et al. Ferromagnetic resonance study of biogenic ferrihydrite nanoparticles: spin-glass state of surface spins. JETP Lett 2020;111:183. https://doi.org/10.1134/S0021364020030145.
[59] Goya GF, Berquó TS, Fonseca FC, Morales MP. Static and dynamic magnetic properties of spherical magnetite nanoparticles. J Appl Phys 2003;94(5):3520–8. https://doi.org/10.1063/1.1599959.
[60] Shim H, Dutta P, Seehra MS, Bonevich J. Size dependence of the blocking temperatures and electron magnetic resonance spectra in NiO nanoparticles. Solid State Commun 2008;145(4):192–6. https://doi.org/10.1016/j.ssc.2007.10.026.
[61] Nadeem K, Krenn H, Traussnig T, Würschum R, Szabó DV, Letofsky-Papst I. Effect of dipolar and exchange interactions on magnetic blocking of maghemite nanoparticles. J Magn Magn Mater 2011;323(15):1998–2004. https://doi.org/10.1016/j.jmmm.2011.02.041.
[62] Russier V. Blocking temperature of interacting magnetic nanoparticles with uniaxial and cubic anisotropies from Monte Carlo simulations. J Magn Magn Mater 2016;409:50–5. https://doi.org/10.1016/j.jmmm.2016.02.070.
[63] Afremov LL, Anisimov SV, Iliushin IG. Modeling of the blocking temperature of a system of core/shell nanoparticles. Chin J Phys 2021;70:324–35. https://doi.org/10.1016/j.cjph.2020.06.022.
[64] Balaev DA, Semenov SV, Dubrovskiy AA, Yakushkin SS, Kirillov VL, Martyanov ON. Superparamagnetic blocking of an ensemble of magnetite nanoparticles upon interparticle interactions. J Magn Magn Mater 2017;440:199–202. https://doi.org/10.1016/j.jmmm.2016.12.046.
[65] Balaev DA, Dubrovskiy AA, Yakushkin SS, Bukhtiyarova GA, Martyanov ON. Temperature of the magnetic ordering of the trivalent iron oxide ε-Fe_2O_3. Phys Solid State 2019;61(3):345–9. https://doi.org/10.1134/S1063783419030053.
[66] Meneses CT, Duque JGS, de Biasi E, Nunes WC, Sharma SK, Knobel M. Competing interparticle interactions and surface anisotropy in NiO nanoparticles. J Appl Phys 2010;108:013909. https://doi.org/10.1063/1.3459890.
[67] De Biasi E, Ramos CA, Zysler RD, Romero H. Ferromagnetic resonance in amorphous nanoparticles. Phys B 2004;354(1-4):286–9.
[68] Silva FG, Depeyrot J, Raikher YL, Stepanov VI, Poperechny IS, Aquino R, et al. Exchange bias and magnetic anisotropy fields in core–shell ferrite nanoparticles. Scientific Rep 2021;11:5474. https://doi.org/10.1038/s41598-021-84843-0.
[69] Berger R, Bissey J-C, Kliava J, Berger R, Bissey J-C. Lineshapes in magnetic resonance spectra. J Phys: Condens Matter 2000;12(44):9347–60. https://doi.org/10.1088/0953-8984/12/44/315.
[70] Landers J, Stromberg F, Darbandi M, Schöppner C, Keune W, Wende H. Correlation of superparamagnetic relaxation with magnetic dipole interaction in capped iron-oxide nanoparticles. J Phys: Condens Matter 2015;27(2):026002. https://doi.org/10.1088/0953-8984/27/2/026002.
[71] Gazeau F, Bacri JC, Gendron F, Perzynski R, Raikher YL, Stepanov VI, et al. Magnetic resonance of ferrite nanoparticles: evidence of surface effects. J Magn Magn Mater 1998;186(1-2):175–87. https://doi.org/10.1016/S0304-8853(98)00080-8.
[72] Berger R, Bissey J-C, Kliava J, Daubric H, Estournès C. Temperature dependence of superparamagnetic resonance of iron oxide nanoparticles. J Magn Magn Mater 2001;234(3):535–44. https://doi.org/10.1016/S0304-8853(01)00347-X.
[73] Rubinstein M, Kodama RH, Makhlouf SA. Electron spin resonance study of NiO antiferromagnetic nanoparticles. J Magn Magn Mater 2001;234(2):289–93. https://doi.org/10.1016/S0304-8853(01)00313-4.
[74] Noginova N, Chen F, Weaver T, Giannelis EP, Bourlinos AB, Atsarkin VA. Magnetic resonance in nanoparticles: between ferro- and paramagnetism. J Phys: Condens Matter 2007;19:246208. https://doi.org/10.1088/0953-8984/19/24/246208.

[75] Domracheva NE, Pyataev AV, Manapov RA, Gruzdev MS. Chem Phys Chem 2011; 12:3009–19. https://doi.org/10.1002/cphc.201100363.

[76] Antoniak C, Lindner J, Farle M. Magnetic anisotropy and its temperature dependence in iron-rich Fe_xPt_{1-x} nanoparticles. Europhys Lett 2005;70(2):250–6. https://doi.org/10.1209/epl/i2004-10485-9.

[77] Pankrats AI, Vorotynov AM, Tugarinov VI, Zharkov SM, Velikanov DA, Abramova GM, et al. Structural and magnetic resonance investigations of CuCr2S4 nanoclusters and nanocrystals. J Appl Phys 2014;116:054302. https://doi.org/10.1063/1.4891993.

[78] Pankrats AI, Vorotynov AM, Tugarinov VI, Zharkov SM, Zeer GM, Ramasamy K, et al. Magnetic resonance studies of mixed chalcospinel $CuCr_2S_xSe_{4-x}$ (x = 0; 2) and $Co_xCu_{1-x}Cr_2S_4$ (x = 0.1; 0.2) nanocrystals with strong interparticle interactions. J Magn Magn Mater 2018;452:297–305. https://doi.org/10.1016/j.jmmm.2017.12.092.

[79] Edelman IS, Zharkov SM, Pankrats AI, Vorotynov AM, Tugarinov VI, Ivantsov RD, et al. Electron spin resonance in $Cu_{1-x}FexCr_2Se_4$ nanoparticles synthesized with the thermal decomposition method. J Magn Magn Mater 2017;436:21–30. https://doi.org/10.1016/j.jmmm.2017.04.006.

[80] Yakovlev IV, Yakushkin SS, Kazakova MA, Trukhan SN, Volkova ZN, Gerashchenko AP, et al. Superparamagnetic behaviour of metallic Co nanoparticles according to variable temperature magnetic resonance. PCCP 2021; 23(4):2723–30. https://doi.org/10.1039/D0CP05963C.

[81] Sova KY, Vakula AS, Tarapov SI, Belous AG, Solopan SO. Analysis of low-temperature FMR spectra of Fe_3O_4 and $ZnFe_2O_4$ nanoparticles synthesized using organic molecules. Low Temp Phys 2021;47(3):220–7. https://doi.org/10.1063/10.0003522.

[82] Mosiniewicz-Szablewska E, Ślawska-Waniewska A, Świątek K, Nedelko N, Galązka-Friedman J, Friedman A. Electron paramagnetic resonance studies of human liver tissues. Appl Magn Reson 2003;24(3-4):429–35.

[83] Punnoose A, Seehra MS, van Tol J, Brunel LC. High-frequency electron magnetic resonance and magnetic studies of ferrihydrite nanoparticles and evidence of a phase transition. J Magn Magn Mater 2005;288:168. https://doi.org/10.1016/j.jmmm.2004.09.003.

[84] Wencka M, Jelen A, Jagodič M, Khare V, Ruby C, Dolinšek J. Magnetic and EPR study of ferric green rust-and ferrihydrite-coated sand prepared by different synthesis routes. J Phys D Appl Phys 2009;42:245301. https://doi.org/10.1088/0022-3727/42/24/245301.

[85] Yurtaeva SV, Efimov VN, Silkin NI, Rodionov AA, Burmistrov MV, Panov AV, et al. Magnetic resonance of ferritin crystalline particles in tumor tissue. Appl Magn Reason 2012;42(3):299–311. https://doi.org/10.1007/s00723-012-0312-2.

[86] Stolyar SV, Yaroslavtsev RN, Iskhakov RS, Bayukov OA, Balaev DA, Dubrovskii AA, et al. Magnetic and resonance properties of ferrihydrite nanoparticles doped with cobalt. Phys Solid State 2017;59(3):555–63. https://doi.org/10.1134/S1063783417030301.

[87] Knyazev YV, Balaev DA, Stolyar SV, Krasikov AA, Bayukov OA, Volochaev MN, et al. Interparticle magnetic interactions in synthetic ferrihydrite: Mössbauer spectroscopy and magnetometry study of the dynamic and static manifestations. J Alloy Compd 2021;889:161623. https://doi.org/10.1016/j.jallcom.2021.161623.

[88] Anghel L, Balasoiu M, Ishchenko LA, Stolyar SV, Kurkin TS, Rogachev AV, et al. Characterization of bio-synthesized nanoparticles produced by Klebsiella oxytoca. J Phys Conf Ser 2012;351:012005. https://doi.org/10.1088/1742-6596/351/1/012005.

[89] Stolyar S, Bayukov O, Balaev D, Iskhakov R, Ishchenko L, Ladygina V, et al. Production and magnetic properties of biogenic ferrihydrite nanoparticles. J Optoelectron Adv Mater 2015;17:968–72.

[90] Knyazev YV, Balaev DA, Stolyar SV, Bayukov OA, Yaroslavtsev RN, Ladygina VP, et al. Magnetic anisotropy and core-shell structure origin of the biogenic ferrihydrite nanoparticles. J Alloy Compd 2021;851:156753. https://doi.org/10.1016/j.jallcom.2020.156753.

[91] Velikanov DA. SQUID magnetometer for investigations of the magnetic properties of materials in the temperature range 4.2-370 K. Sib J Sci Technol 2013;2(48):176.

[92] Balaev AD, Boyarshinov YV, Karpenko MM, Khrustalev BP. Automated magnetometer with superconducting solenoid. Prib Tekh Eksp 1985;3:167.

[93] Tugarinov VI, Makievskii IY, Pankrats AI. Instruments. Exp Tech 2004;47(4):472.

[94] Van der Woude F, Dekker AJ. The relation between magnetic properties and the shape of mössbauer spectra. Phys Status Solidi B 1965;9(3):775–86. https://doi.org/10.1002/pssb.19650090314.

[95] Wickman HH, Klein MP, Shirley DA. Paramagnetic hyperfine structure and relaxation effects in Mössbauer spectra: Fe^{57} in ferrichrome A. Phys Rev 1966;152 (1):345. https://doi.org/10.1103/PhysRev.152.345.

[96] Fabris F, Kun-Hua Tu, Ross CA, Nunes WC, Influence of dipolar interactions on the magnetic properties of superparamagnetic particle systems, J Appl Phys 126 (2019) 173905; 10.1063/1.512559.

[97] Caruntu D, Caruntu G, O'Connor CJ. Magnetic properties of variable-sized Fe3O4 nanoparticles synthesized from non-aqueous homogeneous solutions of polyols. J Phys D Appl Phys 2007;40:5801–9. https://doi.org/10.1088/0022-3727/40/19/001.

[98] Komogortsev SV, Iskhakov RS, Fel'k VA. Fractal dimension effect on the magnetization curves of exchange-coupled clusters of magnetic nanoparticles. J Exp Theor Phys 2019;128:754–60. https://doi.org/10.1134/S1063776119040095.

[99] Komogortsev SV, Fel'k VA, Li OA. The magnetic dipole-dipole interaction effect on the magnetic hysteresis at zero temperature in nanoparticles randomly dispersed within a plane. J Magn Magn Mater 2019;473:410–5. https://doi.org/10.1016/j.jmmm.2018.10.091.

[100] Silva NJO, Millan A, Palacio F, Kampert E, Zeitler U, Amaral VS. Temperature dependence of antiferromagnetic susceptibility in ferritin. Phys Rev B 2009;79:104405. https://doi.org/10.1103/PhysRevB.79.104405.

[101] Balaev DA, Popkov SI, Krasikov AA, Balaev AD, Dubrovskiy AA, Stolyar SV, et al. Temperature behavior of the antiferromagnetic susceptibility of nanoferrihydrite from the measurements of the magnetization curves in fields of up to 250 kOe. Phys Solid State 2017;59(10):1940–6. https://doi.org/10.1134/S1063783417100031.

[102] Néel L. Superantiferromagnetism in small particles. CR Acad Sci Paris 1961;253:203.

[103] Mørup S, Madsen DE, Frandsen C, Bahl CRH, Hansen MF. Experimental and theoretical studies of nanoparticles of antiferromagnetic materials. J Phys: Condens Matter 2007;19(21):213202. https://doi.org/10.1088/0953-8984/19/21/213202.

[104] Bødker F, Hansen MF, Bender Koch C, Mørup S. Particle interaction effects in antiferromagnetic NiO nanoparticles. J Magn Magn Mater 2000;221(1-2):32–6. https://doi.org/10.1016/S0304-8853(00)00392-9.

[105] Mørup S, Hansen MF, Frandsen C. Magnetic interactions between nanoparticles. Beilstein J Nanotechnol 2010;1:182–90. https://doi.org/10.3762/bjnano.1.22.

[106] Knyazev YV, Balaev DA, Kirillov VL, Bayukov OA, Mart'yanov ON. Mössbauer Spectroscopy Study of the Superparamagnetism of Ultrasmall ϵ-Fe_2O_3 Nanoparticles. JETP Lett 2018;108:527–31. https://doi.org/10.1134/S0021364018200092.

[107] Duarte EL, Itri R, Lima Jr E, Baptista MS, Berquó TS, Goya GF. Large magnetic anisotropy in ferrihydrite nanoparticles synthesized from reverse micelles. Nanotechnol 2006;17:5549–55. https://doi.org/10.1088/0957-4484/17/22/004.

[108] Berquó TS, Erbs JJ, Lindquist A, Penn RL, Banerjee SK. Effects of magnetic interactions in antiferromagnetic ferrihydrite particles. J Phys: Condens Matter 2009;21(17):176005. https://doi.org/10.1088/0953-8984/21/17/176005.

[109] Djurberg C, Svedlindh P, Nordblad P, Hansen MF, Bødker F, Mørup S. Dynamics of an interacting particle system: evidence of critical slowing down. Phys Rev Lett 1997;79(25):5154–7. https://doi.org/10.1103/PhysRevLett.79.5154.

[110] Nadeem K, Kamran M, Javed A, Zeb F, Hussain SS, Mumtaz M, et al. Role of surface spins on magnetization of Cr_2O_3 coated γ-Fe_2O_3 nanoparticles. Solid State Sci 2018;83:43–8. https://doi.org/10.1016/j.solidstatesciences.2018.07.006.

[111] Suzuki M, Fullem SI, Suzuki IS, Wang L, Zhong C-J. Observation of superspin-glass behavior in Fe_3O_4 nanoparticles. Phys Rev B 2009;79:024418. https://doi.org/10.1103/PhysRevB.79.024418.

[112] Nunes WC, Socolovsky LM, Denardin JC, Cebollada F, Brandl AL, Knobel M. Role of magnetic interparticle coupling on the field dependence of the superparamagnetic relaxation time. Phys Rev B 2005;72:212413. https://doi.org/10.1103/PhysRevB.72.212413.

[113] Knobel M, Nunes WC, Winnischofer H, Rocha TCR, Socolovsky LM, Mayorga CL, et al. Effects of magnetic interparticle coupling on the blocking temperature of ferromagnetic nanoparticle arrays. J Non-Cryst Solids 2007;353(8-10):743–7. https://doi.org/10.1016/j.jnoncrysol.2006.12.037.

[114] Nogués J, Schuller IK. Exchange bias. J Magn Magn Mater 1999;192(2):203–32. https://doi.org/10.1016/S0304-8853(98)00266-2.

[115] Nogués J, Sort J, Langlais V, Skumryev V, Suriñach S, Muñoz JS, et al. Exchange bias in nanostructures. Phys Rep 2005;422:65. https://doi.org/10.1016/j.physrep.2005.08.004.

[116] Malozemoff AP. Mechanisms of exchange anisotropy (invited). J Appl Phys 1988; 63(8):3874–9. https://doi.org/10.1063/1.340591.

[117] Nagata K, Ishikara A. ESR of ultrafine magnetic particles. J Magn Magn Mater 1992;104–107:1571–3. https://doi.org/10.1016/0304-8853(92)91459-7.

[118] Komogortsev SV, Balaev DA, Krasikov AA, Stolyar SV, Yaroslavtsev RN, Ladygina VP, et al. Magnetic hysteresis of blocked ferrihydrite nanoparticles. AIP Adv 2021;11:015329. https://doi.org/10.1063/9.0000111.

[119] Popkov SI, Krasikov AA, Semenov SV, Dubrovskii AA, Yakushkin SS, Kirillov VL, et al. General regularities and differences in the behavior of the dynamic magnetization switching of ferrimagnetic ($CoFe_2O_4$) and antiferromagnetic (NiO) nanoparticles. Phys Solid State 2020;62(9):1518–24. https://doi.org/10.1134/S1063783420090255.